Bergische Universität Wuppertal

Fakultät für Mathematik und Naturwissenschaften

Institute of Mathematical Modelling, Analysis and Computational Mathematics (IMACM)

Preprint BUW-IMACM 26/04

Matthias Ehrhardt, Sergey Pereselkov, Venedikt Kuz'kin,
Sergey Tkachenko and Alexey Pereselkov

Frequency Variations Of Two Modes Interference Patterns Due To Internal Soliton Wave In Shallow Water

March 26, 2026

http://www.imacm.uni-wuppertal.de

Article

Frequency Variations Of Two Modes Interference Patterns Due To Internal Soliton Wave In Shallow Water

Matthias Ehrhardt[1,*], Sergey Pereselkov[2], Venedikt Kuz'kin[3], Sergey Tkachenko[2] and Alexey Pereselkov[2]

[1] University of Wuppertal, Chair of Applied and Computational Mathematics, Gaußstraße 20, 42119 Wuppertal, Germany; ehrhardt@uni-wuppertal.de
[2] Voronezh State University, Mathematical Physics and Information Technology Department, 394018 Voronezh, Russia; pereselkov@yandex.ru (S.P.); tkachenko.edu@yandex.ru (S.T.); pereselkov.edu@yandex.ru (A.P.)
[3] Prokhorov General Physics Institute of the Russian Academy of Sciences, 119991, Moscow, Russia; kumiov@yandex.ru
* Correspondence: ehrhardt@uni-wuppertal.de

Abstract: This paper investigates frequency shifts in the interference structure of acoustic fields caused by internal-wave solitons in shallow-water environments. A coupled-mode framework is developed to describe the interaction of acoustic normal modes under soliton-induced perturbations of the refractive index. In the weak coupling regime, analytical expressions are derived for modal phase variations and the resulting frequency shifts, providing physical insight into the mechanisms that govern interference modulation. The theoretical results are supported by numerical simulations under realistic ocean conditions. These simulations demonstrate that soliton-induced mode coupling produces oscillatory patterns in the frequency-shift spectrum that depend strongly on soliton properties and modal structure. Based on these findings, we propose an inverse approach to estimate key soliton parameters, such as propagation direction, velocity, and effective amplitude, from observed frequency shifts. The results underscore the potential of frequency-shift analysis as a practical, robust tool for remotely sensing internal-wave dynamics in ocean acoustics.

Keywords: internal soliton waves; KdV-equation; sound field; mode coupling; interference pattern; frequency shift; shallow water; waveguide

1. Introduction

Research on interference patterns formed by acoustic fields in oceanic waveguides is a fundamental topic in underwater acoustics [1,2]. The spatial-frequency structure of these patterns contains essential information about waveguide properties, source characteristics, and environmental perturbations, thereby motivating interest in the topic. A major advance in interpreting frequency-range striations and related interference effects was achieved through the concept of the waveguide invariant [2], which established a unified framework for analyzing them in both modal and ray-based descriptions [3–6]. Subsequent studies have extended this framework to more realistic and complex scenarios, including range-dependent environments, receiver-depth effects, thermocline influence, and mode coupling [7–12]. More recent investigations have shown that interference structure analysis can be applied to deep-water waveguides, where the waveguide invariant is more appropriately treated as a distributed rather than constant parameter [10,13]. Taken together, these studies demonstrate that interference patterns are a physically informative tool for acoustic diagnostics and interferometric signal processing, not merely a manifestation of multipath propagation.

In recent years, increasing attention has been paid to *interferometric signal processing* (ISP) in underwater acoustics because it provides an effective framework for extracting physically meaningful information from broadband acoustic fields in ocean waveguides [14–16]. Several influential studies developed the core theoretical ideas and methodological basis of ISP, defining the principal concepts

of this approach and revealing its usefulness for underwater acoustic diagnostics [14–16]. Subsequent work has demonstrated ISP's effectiveness in a wide range of practical applications. In particular, ISP-based techniques have been used to estimate waveguide-invariant parameters [17,18]. . These techniques have also been confirmed to be effective in analyzing weak signals, especially when combined with array beamforming to improve signal detectability [19]. Additionally, ISP has been used for seabed characterization based on acoustic emissions from passing ships [20] and for estimating source range in shallow-water environments [21]. A method for range-independent invariant estimation within the ISP framework was introduced in [22], whereas [23] considered the interpretation of interference fringes in terms of eigenray or eigenbeam arrival times. Furthermore, ISP has been adapted for passive sonar applications in deep-water settings [24,25]. Overall, these studies demonstrate that the ISP approach is flexible and provides valuable physical information for analyzing acoustic fields in a wide range of underwater waveguide environments.

Among ISP-based techniques, *holographic signal processing* (HSP) is one of the most promising directions [26,27]. The underlying physical concepts and mathematical formulation of hologram construction were first introduced in [26]. In the HSP approach, the quasi-coherent integration of acoustic intensity in the frequency-time domain results in the formation of an interferogram. This accumulated intensity distribution is analyzed by applying a classical two-dimensional Fourier transform (2D-FT) [26] or fractional Fourier transform (FrFT) [28] to the interferogram. The resulting quantity is commonly referred to as the *Fourier hologram*, or simply the hologram. In this representation, the acoustic energy contained in the interferogram is localized into focal regions formed in the hologram domain as a result of the interference of different propagating modes of the sound field. This process is analogous to the spatial focusing of wave fields achieved by wavefront reversal and time-reversal techniques [29], but it does not require extended receiver arrays or occur in the physical space of the waveguide. Instead, focusing occurs in the frequency-time domain of the hologram. HPS is a viable alternative to the traditional *matched field processing* (MFP) approach [30–34]. Despite its broad use in underwater acoustics, MFP's practical performance depends heavily on precise a priori information about the propagation environment, including detailed descriptions of the water column and seabed characteristics [30,31]. In shallow-water waveguides, however, environmental information is often limited or uncertain. Variability associated with internal waves, tides, and changes in stratification can cause substantial model mismatch, reducing the effectiveness of MFP [32,33]. In contrast, the proposed holographic approach relies less on precise environmental knowledge and remains efficient even when information about the waveguide is incomplete. This makes it a promising tool for adaptive acoustic sensing in complex marine conditions [34].

In the early stages of HSP development, the waveguide was typically considered stationary in space and time. In practice, however, acoustic propagation often occurs in waveguides that are subject to hydrodynamic disturbances. The feasibility of applying HSP to a stationary source under realistic ocean conditions was first examined in a series of experiments [35–38]. These studies demonstrated that hydrodynamic inhomogeneities deform the interferogram and cause the focal regions in the corresponding hologram to broaden. Under these conditions, the hologram can be interpreted as the sum of two components: one associated with the unperturbed waveguide and one produced by the perturbations. This two-component representation was used in [35–38] to interpret experimental results obtained in the SWARM'95 experiment [39–41]. The waveguide inhomogeneities observed during SWARM'95 were mainly related to *internal soliton waves* (ISWs), which are among the most common hydrodynamic processes in the ocean [42–44]. Two acoustic tracks were used in the SWARM'95 experiment; both were generated by a single source and recorded by two vertically separated receiving arrays. The first track was oriented at a small angle relative to the ISW front. In this geometry, ISW structures produced strong horizontal refraction of acoustic rays. In a previous study [46], we investigated changes in the hologram structure for a moving source under conditions of pronounced horizontal ray refraction caused by ISWs. In contrast, the second acoustic track in SWARM'95 was directed across the ISW front so that the waves would propagate along the source-

receiver path. In this configuration, the dominant effect was not horizontal refraction, but rather, substantial redistribution of acoustic energy between propagating modes, i.e., mode coupling. This mechanism was addressed in our earlier paper [47]. That paper [47] presents a detailed analysis of the influence of ISWs propagating along the acoustic path on the hologram structure of a moving source. Identifying the characteristic features of variations in the source interferogram structure caused by strong ISW-induced mode coupling is essential for further developing HSP. For this reason, the present paper focuses on analyzing this effect.

This paper investigates the influence of ISWs on the interferogram of a source sound field in shallow water. The study focuses on cases where the ISWs propagate along the acoustic path between the source and receiver, causing significant coupling between acoustic modes. The study is based on numerical simulations that explicitly account for mode coupling induced by internal wave activity. Within this framework, we examine variations in the interferogram – that is, the received sound intensity distribution in the frequency-time domain – under space-time inhomogeneities produced by ISWs. One of the paper's main results is a theory of frequency shifts in two-mode interference patterns, verified by numerical simulations. Within the proposed framework, we analyze frequency shifts arising from ISW-induced coupling between two propagating normal modes in a shallow-water waveguide. We also assess the diagnostic potential of these shifts and evaluate the applicability of this approach to inverse estimation of soliton parameters and analysis of oceanic inhomogeneities. This is done under conditions where normal modes can no longer be treated as independent.

This study uses numerical modeling to analyze the propagation of sound in three-dimensional (3D) inhomogeneous shallow-water waveguides. Under these conditions, the acoustic field's structure can substantially change due to 3D environmental inhomogeneities caused by internal wave (ISW)-induced scattering. Simulating broadband, low-frequency sound fields in these environments is computationally demanding and typically requires advanced numerical methods and high-performance computing resources to achieve physically reliable solutions. Existing numerical approaches for simulating sound propagation in inhomogeneous shallow-water waveguides commonly fall into five categories: [48]: models based on the 3D Helmholtz equation (3DHE) [49–51]; models based on the 3D parabolic equation (3DPE) [52–58]; three-dimensional ray-based (3DR) models [59,60,78]; approaches based on vertical modes and the 2D modal parabolic equation (VMMPE) [45,46,61–63]; and models employing vertically coupled modes with horizontal rays (VCMHR) [64–77].

In this paper, we examine the propagation of low-frequency acoustics in the 90–120 Hz band. We assume that the spatial variability of the shallow-water waveguide is primarily associated with ISWs propagating along the acoustic path between the source and receiver. These ISW-induced inhomogeneities produce significant scattering effects and must therefore be considered in the numerical description of the sound field. Of the five classes of numerical approaches outlined above, the VCMHR model is the most appropriate for this problem. The VCMHR model is specifically suited to low-frequency sound propagation in shallow-water waveguides influenced by ISWs, which is why it is the most appropriate choice for this problem. In particular, the VCMHR model adequately treats the boundary conditions while reproducing the essential physical mechanism of vertical mode coupling caused by environmental inhomogeneity. This feature is especially important for the present study, in which mode coupling plays a central role in the transformation of the acoustic field. Fully three-dimensional models are generally more advantageous for higher-frequency applications but less efficient for describing low-frequency mode-coupling effects in shallow water. The 3DHE and 3DPE approaches can deliver highly accurate solutions, but they are not applicable to the present problem due to the high computational cost of solving a fully 3D propagation problem. VMMPE models are effective at describing horizontal refraction but do not sufficiently represent mode coupling, one of the key mechanisms examined in this work. For these reasons, the VCMHR approach was selected as the most suitable numerical framework for simulating sound propagation in a shallow-water waveguide perturbed by ISWs.

The paper models the shallow-water waveguide as a medium whose spatial and temporal variability is governed by ISWs. The simulations are based on the assumption that the speed of an acoustic wave ($\sim$ 1500 m/s) is significantly higher than the speed at which ISWs propagate ($\sim$ 0.5–1 m/s). This difference in characteristic velocities justifies the use of the "frozen environment" approximation [78,79], in which the medium is assumed to remain effectively unchanged during acoustic propagation between the source and receiver.

The paper is organized as follows. Section 1 provides the introduction. Section 2 describes the three-dimensional model of a shallow-water waveguide in the presence of ISWs propagating along the acoustic path. In Section 3 develops the theory of frequency shifts for the two-mode case. Section 4 presents the numerical results for the frequency shifts of a broadband sound source in a shallow-water waveguide under conditions of significant ISW-induced mode coupling. Section 5 addresses the corresponding inverse problem and demonstrates that it can be solved using information on the frequency shifts of coupled normal modes, contrary to earlier doubts. The main conclusions are given in Section 6.

2. The Shallow Water Waveguide Model

This section introduces a three-dimensional description of the shallow-water acoustic waveguide considered in this work (see Figure 1). The model is formulated in a Cartesian coordinate system (X, Y, Z). The propagation medium is represented by a water layer whose acoustic properties are characterized by a sound speed $c(\mathbf{r}, z, t)$ and a density $\rho(\mathbf{r}, z, t)$, that vary in both space and time. The horizontal location is specified by the vector $\mathbf{r} = (x, y)$. The upper boundary of the domain corresponds to the sea surface located at $z = 0$, and the lower boundary is formed by the ocean bottom at depth $z = H$. The seabed is described by the density parameter ρ_b and by a complex refractive index of the form $n_b(1 + \mathrm{i}\varkappa)$ [78,79]. The quantity $\varkappa$ accounts for acoustic attenuation within the bottom medium and is given by $\varkappa = \chi c_b/(54.6f)$. In this equation, the bottom loss coefficient is denoted by χ, the sound speed in the bottom material is denoted by c_b and the acoustic frequency is denoted by f.

The spatial and temporal variability of the acoustic properties of the water column can be represented as follows [78,79]:

$$c(\mathbf{r}, z, t) = \bar{c}(z) + \tilde{c}(\mathbf{r}, z, t), \tag{1}$$

where $\bar{c}(z)$ denotes the reference sound-speed profile characterizing the medium when internal wave processes are absent. The term $\tilde{c}(\mathbf{r}, z, t)$ represents the fluctuations of the sound speed caused by the presence of *internal soliton waves* (ISWs).

Using Equation (1), the square of the refractive index within the water column can be written as [78,79]:

$$n^2(\mathbf{r}, z, t) = \bar{n}^2(z) + \tilde{n}^2(\mathbf{r}, z, t), \tag{2}$$

where $\bar{n}^2(z)$ represents the background refractive-index distribution corresponding to the undisturbed medium and $\tilde{n}^2(\mathbf{r}, z, t)$ describes the variation produced by ISWs. According to the approach presented in [44,45], the perturbation term can be expressed as

$$\tilde{n}^2(\mathbf{r}, z, t) = -2QN^2(z)\hat{\Phi}(z)\zeta(\mathbf{r}, t), \tag{3}$$

where $Q \approx 2.4\ \mathrm{s}^2/\mathrm{m}$ is a constant that depends on the physical properties of seawater. The quantity $N(z) = \left(-\frac{g}{\rho}\frac{d\rho}{dz}\right)^{1/2}$ denotes the buoyancy (Brunt–Väisälä) frequency, $\hat{\Phi}(z)$ is the eigenfunction of the first internal-gravity mode, normalized to unity at termocline depth and $\zeta(\mathbf{r}, t)$ characterizes the vertical displacement of termocline water layer generated by ISWs.

ISWs are commonly observed in oceanic environments. They appear as sequences of short-period vertical oscillations of stratified water layers and can be interpreted as packets of internal solitary waves that propagate toward the continental shelf. ISW generation is typically associated with internal tidal processes [42–44]. Representative characteristics of these waves, obtained from experimental

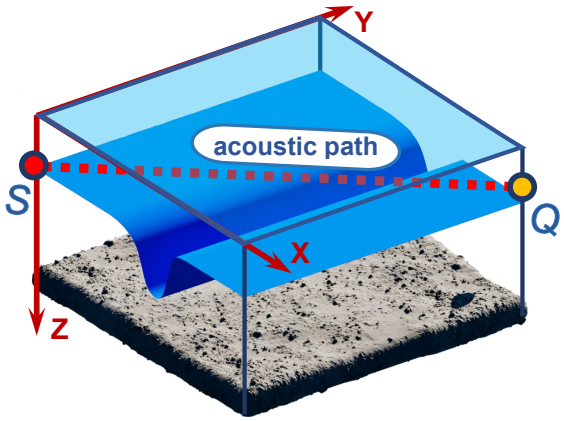

Figure 1. Model of a shallow water waveguide at presence of ISWs: S – source, Q – receiver, dashed line – source-receiver path.

observations, are summarized in Table 1 [39,40,42–44]. These parameters give rise to distinct acoustic effects in the marine environment.

According to the reported results [45], when ISWs intersect the acoustic track between a source and a receiver, they significantly impact the horizontal refraction of acoustic rays propagating at small angles relative to the wavefronts of the internal waves. Consequently, time-dependent horizontal waveguides are formed, whose axes are oriented approximately parallel to the ISW fronts. We analyzed the influence of this phenomenon on the holographic pattern produced by a moving acoustic source in our earlier works, for example [46]. In contrast, when ISWs propagate along the acoustic path between the source and receiver, pronounced coupling occurs between acoustic normal modes [47]. This modes coupling redistributes acoustic energy among the modes and modifies the relative amplitudes that determine the structure of the resulting sound field.

Table 1. ISW Parameters

Parameter	Value
ISW amplitude	$A \sim 10$–$30\,\mathrm{m}$
ISW half-width	$L \sim 100$–$200\,\mathrm{m}$
ISW velocity	$v \sim 0.5$–$1\,\mathrm{m/s}$
ISW curvature radius	$R \sim 15$–$25\,\mathrm{km}$

The vertical displacement of fluid parcels caused by a soliton can be described by the Korteweg–de Vries (KdV) equation, where the displacement field takes the form [44,45]:

$$\zeta(x) = A\ \mathrm{sech}^2\left(\frac{x - vt}{L}\right), \tag{4}$$

where A is the soliton amplitude and L characterizes its half-width at the level of 0.42 of the maximum value.

For analytical convenience, this profile (4) is approximated by a rectangular pulse:

$$\zeta(x) = A\ \mathrm{rect}\left(\frac{x}{L}\right) = \begin{cases} A, & |x/L| \le 1, \\ 0, & |x/L| > 1. \end{cases} \tag{5}$$

This approximation (5) is based on the assumption that the excitation energies of the original and simplified pulses are identical. Accordingly, the areas under the two profiles are considered equal:

$$A \int_{-\infty}^{\infty} \mathrm{sech}^2\left(\frac{x}{L}\right) dx = A \int_{-L}^{L} \mathrm{rect}\left(\frac{x}{L}\right) dx = 2AL. \tag{6}$$

This substitution allows us to disregard the variation in scattering characteristics within the inhomogeneous region.

Figure 2 illustrates the two idealized initial ISW shapes considered in the paper Equation (4) and Equation (5). Panel 2(a) shows a squared hyperbolic secant profile representing the KdV solution for an ISW, with a maximum displacement of $A = 15$ m at the ISW crest and a gradual decay toward zero away from the ISW crest. Panel 2(b) presents an approximate rectangular profile with the same amplitude, $A = 15$ m, characterized by a uniform displacement within the central region and sharp transitions at the ISW edges. The parameter L is 100 m for both profiles.

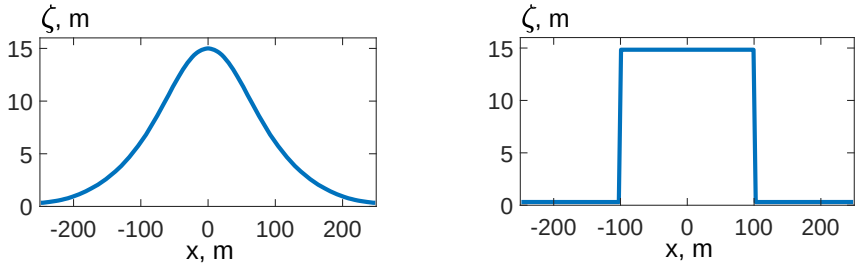

Figure 2. ISW shape. **(a)** squared hyperbolic secant (KdV-solution) shape; **(b)** approximate rectangular shape. ISW parameters: $A = 15\,m$, $L = 100\,m$.

Table 2. Shallow water waveguide parameters

Parameter	**Value**
Waveguide depth	70 m
Bottom refractive index	$n_b = 0.82\,(1 + \mathrm{i}\,0.01)$
Bottom density	$\rho_b = 1.8\,\mathrm{g/cm^3}$
Modes count	$M = 2$
Source depth	$z_0 = 30\,\mathrm{m}$
Receiver depth	$z_0 = 30\,\mathrm{m}$
Source-receiver range	$r_0 = 10\,\mathrm{km}$
Frequency band	$\Delta f = 90$–$120\,\mathrm{Hz}$

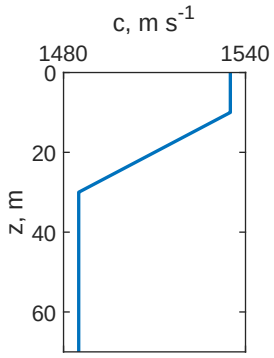

Figure 3. Sound speed dependence in a shallow water waveguide in the absence of ISWs.

The adequacy of this theoretical model was verified through numerical simulations of frequency-shift processes in Section 4 in these two representative cases. The modeling was carried out using the following parameters (see Table 2). The undisturbed sound-speed profile versus depth with thermocline is shown in Figure 3. The bottom parameters were set as follows: the ratio of bottom sediment density to water density $\rho_b/\rho = 1.8$, and the complex refractive index $n_b = 0.82\,(1 + \mathrm{i}\,0.01)$. In the frequency range of 90–120 Hz, modal groups with nearly identical amplitudes were studied,

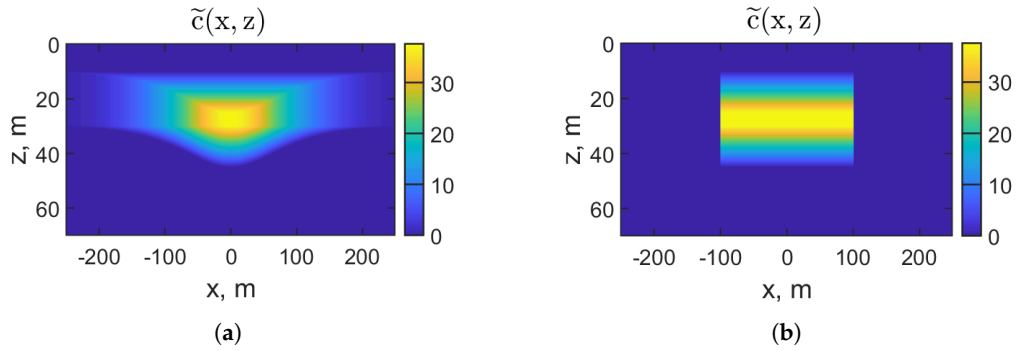

Figure 4. Space variations of the sound speed $\tilde{c}(x,z)$ due to ISW: **(a)** squared hyperbolic secant (KdV-solution) shape; **(b)** approximate rectangular shape. ISW parameters: $A = 15\,\text{m}$, $L = 100\,\text{m}$.

with a spectral discretization of $\delta f = 0.2\,\text{Hz}$. The acoustic source and receiver were located at a depth of $z_0 = 30\,\text{m}$, and the horizontal propagation distance was $r_0 = 10\,\text{km}$.

The soliton was modeled as a squared hyperbolic secant pulse with the following parameters: amplitude $A = 15\,\text{m}$, half-width $L = 100\,\text{m}$, and velocity $v = 1\,\text{m/s}$.

Figure 4 shows the spatial variations of the sound-speed perturbation $\tilde{c}(x,z)$ associated with two idealized ISW profiles and for undisturbed sound-speed profile shown in Figure 3. In panel 4(a), corresponding to the squared hyperbolic secant KdV-solution shape for ISW, the perturbation field is smoothly distributed around the wave core, with the largest values concentrated in the upper part of the domain near the wave center and a gradual decay in both the horizontal and vertical directions. In contrast, panel 4(b) displays the perturbation field generated by the approximate rectangular ISW profile, where the region of elevated $\tilde{c}(x,z)$ is more horizontally uniform and confined, with comparatively sharp boundaries at the wave edges.

The coupling between the first and second modes of the acoustic field ($m = 1$, $n = 2$) was analyzed, because this pair exhibits the strongest coupling. To track frequency shift dynamics, a narrow-band local source with a known spectral position within the given frequency band was used.

3. Frequency Shifts Theory. Two Modes Case.

This section presents the theory of frequency shifts for a sound field consisting of two modes. The section is divided into four parts. Subsection 3.1 describes a sound field consisting of two modes in a shallow-water waveguide in the presence of ISW. Subsection 3.2 examines the coupled modes approximation for frequency shifts. Subsection 3.3 considers the case when the ISW propagates along the source-receiver path (case: $\alpha = 0$). Subsection 3.4 considers the case when the ISW propagates at an angle to the source-receiver path (case: $\alpha \neq 0$).

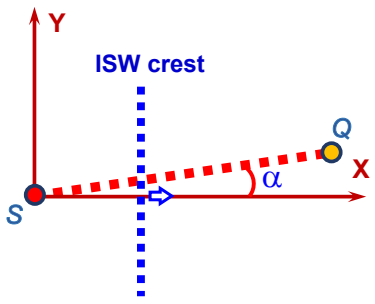

Figure 5. Geometry of the problem: S – source; Q – receiver; red dashed line – source-receiver path; blue dashed line – ISW crest; blue arrow – ISW velocity vector $\mathbf{v}$; angle between source-receiver path and X-axis.

Figure 5 shows the schematic geometry considered in this study. The source and receiver are denoted by S and Q, respectively. The red dashed line corresponds to the source-receiver path, and the blue dashed vertical line marks the crest of the ISW. The blue arrow indicates the ISW's propagation

velocity vector. The angle α is measured between the source-receiver path and the X-axis. In the absence of ISWs, the shallow water waveguide is assumed to be horizontally homogeneous. The width of the ISW front exceeds the length of the source-receiver path. Frequency shifts are analyzed using the quasi-stationary approximation, in which scattering by inhomogeneities occurs as if the perturbation were frozen in time, and the temporal dependence is restored later in the final expressions.

3.1. Sound Field Model in the Presence of ISW

Within the framework of the vertical-mode and horizontal-ray approximations, the sound field represented by two modes can be written as follows [78,79]:

$$p(\mathbf{r}, z) = P_m(\mathbf{r})\phi_m(z) + P_n(\mathbf{r})\phi_n(z). \tag{7}$$

Here, $\mathbf{r} = (x, y)$ is the horizontal position vector, P_m and P_n are the modal amplitudes, and $\phi_m(z)$ and $\phi_n(z)$ describe the vertical structure (mode shapes) of the corresponding acoustic modes in an unperturbed waveguide, i.e., in the absence of an ISW. The complex horizontal wavenumber of each mode is defined as $\xi_m = h_m + \mathrm{i}\gamma_m$, where h_m and γ_m denote its real and imaginary parts, respectively. Consequently, the acoustic pressure field p depends on the angular frequency $\omega = 2\pi f$ and wavenumber $k = \omega/c$.

The eigenfunctions $\phi_m(z)$ and the complex wavenumbers h_m are determined by solving the corresponding Sturm-Liouville eigenvalue problem subject to boundary conditions at the free surface and the bottom [78,79]:

$$\frac{d^2\phi_m(z)}{dz^2} + k^2\bar{n}^2(z)\,\phi_m(z) = \xi_m^2\phi_m(z), \tag{8}$$

$$\phi_m(z)\big|_{z=0} = 0, \qquad \phi_m(z)\big|_{z=H} + g(\xi_m)\frac{d\phi_m(z)}{dz}\Big|_{z=H} = 0, \tag{9}$$

where

$$g(\xi_m) = \eta \Big/ \sqrt{\xi_m^2 - k^2 n_b^2(1 + \mathrm{i}\varkappa)}. \tag{10}$$

We will use the coupled mode approach to account for the scattering of the sound field Equation (7) induced by the inhomogeneities of the water layer caused by ISWs. In the mode amplitude $P_m(\mathbf{r})$, we isolate the factor corresponding to cylindrical spreading:

$$P_m(\mathbf{r}) = \frac{M_m(\mathbf{r})}{\sqrt{h_m r}}, \tag{11}$$

where $M_m(\mathbf{r}) = M_m(r, \alpha)$ denotes the mode amplitude without the cylindrical spreading factor. The horizontal range between the source and receiver is r. This representation explicitly factors out the geometric spreading term $1/\sqrt{r}$, which dominates the range dependence in the shallow water waveguide under consideration. For two coupled modes with indices m and n, the system of equations for the complex amplitudes can be written as follows [78,79]:

$$\begin{cases} \dfrac{dM_m(r,\alpha)}{dr} = \mathrm{i}\mu_{mm}(r,\alpha)\,M_m(r,\alpha) + \mathrm{i}\mu_{mn}(r,\alpha)\,M_n(r,\alpha)\,\exp\left(\mathrm{i}h_{nm}r\right), \\ \dfrac{dM_n(r,\alpha)}{dr} = \mathrm{i}\mu_{nn}(r,\alpha)\,M_n(r,\alpha) + \mathrm{i}\mu_{nm}(r,\alpha)\,M_m(r,\alpha)\,\exp\left(\mathrm{i}h_{mn}r\right), \end{cases} \tag{12}$$

where h_m is the unperturbed value of the real part of the horizontal wavenumber for the m-th mode, $h_{mn} = h_m - h_n$, and μ_{mn} represents the mode coupling coefficient, which is determined by the characteristics of the inhomogeneity. The term describing modal attenuation is omitted here, since numerical simulations indicate that it has no significant effect on the subsequent analysis.

In the case of solitonic inhomogeneities, the coupling coefficients are expressed as:

$$\mu_{mn}(r,\alpha) = -\frac{k^2}{2\sqrt{h_m h_n}} \int_0^H \phi_m(z)\,\phi_n(z)\,\tilde{n}^2(r,\alpha,z)\,dz. \tag{13}$$

The Equations (12) are symmetric with respect to the interchange of lower indices ($m \leftrightarrow n$), so only the first one will be considered further. When the mode indices are identical ($m = n$), the coefficient μ_{mm} equals the linear correction $\tilde{h}_m$ to the unperturbed wavenumber h_m of the m-th mode ($\mu_{mm} = \tilde{h}_m$). For $m \neq n$, we have that $\mu_{mn} = \mu_{nm}$. We use the expression for the perturbation of the squared refractive index $\tilde{n}^2(r,\alpha,z)$ in the form:

$$\tilde{n}^2(r,\alpha,z) = -2QN^2(z)\,\hat{\Phi}(z)\,\zeta(r,\alpha), \tag{14}$$

and thus we can rewrite Equation (13) as

$$\mu_{mn}(r,\alpha) = q_{mn}\,\zeta(r,\alpha), \tag{15}$$

where $\zeta(r,\alpha)$ represents the ISW perturbation function varying in space and time (see Equations (4) and (5)). Continuing from Equation (15), we define the coefficient q_{mn} as

$$q_{mn} = \frac{Qk^2}{\sqrt{h_m h_n}} \int_0^H \phi_m(z)\,\phi_n(z)\,N^2(z)\,\hat{\Phi}(z)\,dz. \tag{16}$$

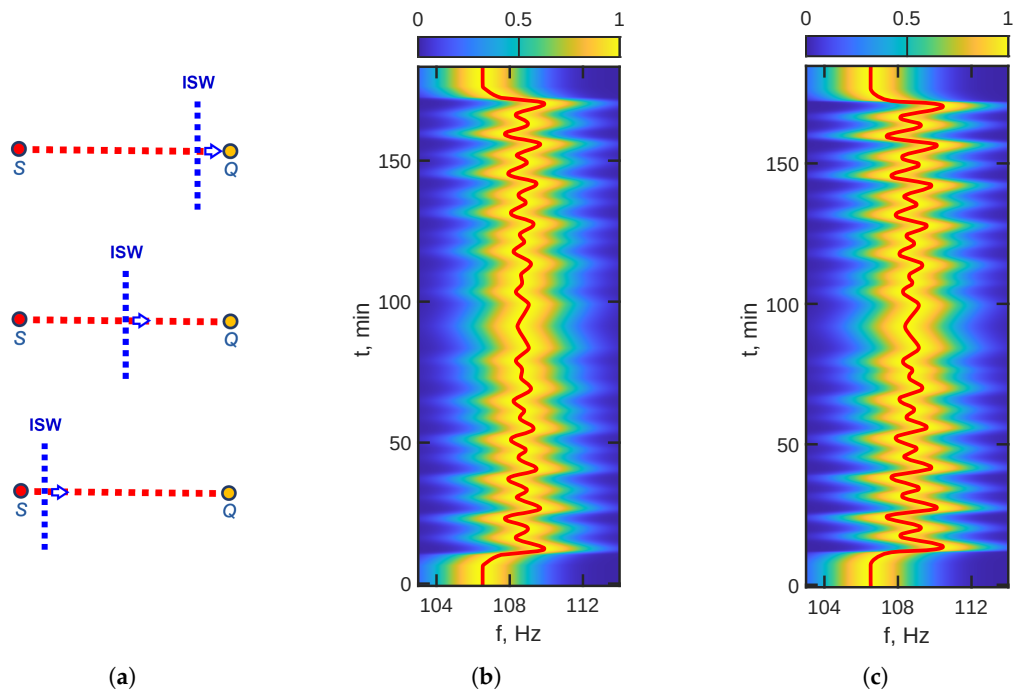

(**a**) (**b**) (**c**)

Figure 6. Frequency shifts due to ISW. **(a)** Scheme of ISW propagation along the source–receiver path. ISW positions at three time moments: $t = 25$ min; $t = 95$ min; $t = 165$. Variations of sound intensity distribution in the frequency-time domain due to ISW motion. **(b)** Squared hyperbolic secant (KdV-solution) shape. **(c)** approximate rectangular shape. ISW parameters: $A = 15$ m, $L = 100$ m, $L = 100$ m, $v = 1$ m/s, $\alpha = 0°$. Red line – variation in the frequency position of interference maxima due to ISW motion.

Figure 6 demonstrates how the propagation of an ISW along the source-receiver path results in the time-dependent restructuring of the acoustic interference pattern. Panel 6(a) presents a schematic of three characteristic ISW positions relative to the fixed source S and receiver Q. These ISW positions correspond to three time points: $t = 25$ min; $t = 95$ min; $t = 165$ min. As the ISW moves along the source-receiver path, it changes the phase relationships among the acoustic modes contributing to

the received field, thereby altering the interference structure of the sound intensity in the frequency domain. Consequently, the positions of the interference maxima in the frequency spectrum become time-dependent at the receiver Q. The corresponding evolution of the interference structure in the frequency-time domain is shown in panels 6(b) and 6(c). In both cases, the background color maps display alternating high- and low-intensity bands associated with constructive and destructive interference. A key feature of these distributions is their gradual displacement along the frequency axis as time increases. This behavior indicates that the characteristic interference frequencies are not fixed, but vary in response to the ISW motion. The red curve traces the temporal evolution of one of the interference maxima, revealing a pronounced oscillatory frequency shift induced by the moving ISW. The frequency shift value $\Omega(t)$ is defined as the difference between the frequency of the interference maximum at a given time $f(t)$ and the frequency of the interference maximum in the absence of an ISW f_0:

$$\Omega(t) = f(t) - f_0. \tag{17}$$

where $\Omega(t)$ is the frequency shift value, $f(t)$ is the frequency of the interference maximum at time t, and f_0 is the frequency of the interference maximum in the absence of an ISW.

Comparing panels 6(b) and 6(c) shows that both ISW representations produce the same general physical effect. In both cases, the interference pattern undergoes smooth, non-monotonic frequency variations throughout the entire observation interval. The two models remain qualitatively and quantitatively consistent and yield nearly identical temporal signatures of the interference maximum frequency variations.

Thus, Figure 6 confirms that ISW motion manifests as measurable frequency shifts of interference fringes in the received acoustic field. These results suggest that the observed spectral variability is determined not only by the presence of the wave itself, but also by its instantaneous position. Therefore, tracking the interference maxima in the frequency-time representation could be a useful tool for diagnosing ISW-induced perturbations and for estimating ISW parameters.

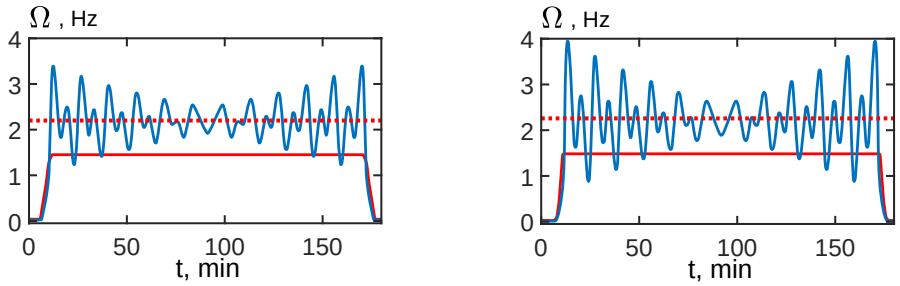

Figure 7. Frequency shifts $\Omega(t)$ due to ISW: **(a)** squared hyperbolic secant (KdV-solution) shape; **(b)** approximate rectangular shape. Red dotted line – mean value of $\Omega(t)$. Red solid line – $\Omega(t)$ without mode coupling. ISW parameters: $A = 15$ m, $L = 100$ m, $v = 1$ m/s, $\alpha = 0$.

Figure 7 presents the temporal behavior of the frequency shift $\Omega(t)$ (Equation (17)) produced by the passage of an ISW for two different representations of the inhomogeneity profile. Panel 7(a) corresponds to the sech^2-type KdV solution, whereas panel 7(b) shows the result obtained for the approximate rectangular shape. In both cases, the frequency shift exhibits a pronounced oscillatory behavior superimposed on a nearly constant mean level while the ISW is on the source-receiver path. Outside this interval, $\Omega(t)$ rapidly decreases to values close to zero, reflecting the disappearance of the ISW's perturbing influence on the propagation conditions.

Comparing panels 7(a) and 7(b) shows that the two modeled wave shapes produce nearly identical temporal signatures of the frequency shift. The duration of the disturbed interval, the mean level of $\Omega(t)$, the amplitude of the oscillations, and the overall envelope of the signal remain nearly unchanged between the two representations. There are only very minor differences in the fine details of the

individual oscillations, but the general structure of the curves is is accurately preserved. Thus, the time dependence of the frequency shift $\Omega(t)$ is primarily determined by the ISW parameters (amplitude A, velocity v, and half-width L), rather than by subtle differences in its profile shape.

This result is important for the subsequent theoretical analysis. The close agreement between the two cases shows that the simplified, approximate rectangular model accurately captures the essential temporal and spectral characteristics of the more realistic sech^2-type ISW with sufficient accuracy. Therefore, using the approximate rectangular shape is justified in the analysis of frequency shifts. This simplification clarifies the theoretical treatment presented in Subsections 3.2, 3.3, and 3.4, while preserving the key physical effects associated with ISW-induced frequency shifts $\Omega(t)$.

3.2. Coupled Modes Approximation for Frequency Shifts

Now, let us consider the theory of frequency shift due to the ISW within the framework of the coupled modes approximation. The solution to system (Equation (12)) determines the complex amplitudes of modes M_m and M_n, which can be expressed as

$$\begin{cases} M_m = M_{m0} + \delta M_m, \\ M_n = M_{n0} + \delta M_n, \end{cases} \tag{18}$$

where M_{m0} and M_{n0} are the initial values of the mode amplitudes in the absence of ISW, and δM_m, δM_n are the amplitude perturbations caused by ISW (Equation (5)). For a point source located at a depth z_0, the quantities M_{m0} and M_{n0} are proportional to the mode eigenfunctions $\phi_m(z_0)$ and $\phi_n(z_0)$, up to a constant factor. The expression for the complex phase Θ_m of the mode amplitude M_m cannot be obtained explicitly for the general case. However, for practical purposes, it is convenient to consider the case of weak coupling, when the relative amplitude perturbations $\psi_m = \delta M_m / M_{m0}$ satisfy $|\psi_m| < 1$, and the problem can be solved analytically. We introduce the logarithm of the complex mode amplitude M_m. Its imaginary part corresponds to the phase shift of the modal amplitude, and its real part represents the logarithm of its magnitude. Expanding $\ln M_m$ into a power series in terms of the small parameter ψ_m, the modal phase Θ_m can be expressed as a series:

$$\Theta_m = \operatorname{Im} \psi_m - \frac{1}{2} \operatorname{Im} \psi_m^2 + \frac{1}{3} \operatorname{Im} \psi_m^3 + \ldots = \Theta_m^{(0)} + \Theta_m^{(1)} + \Theta_m^{(2)} + \ldots. \tag{19}$$

The first term $\Theta_m^{(0)}$ of this expansion represents the linear approximation to the phase perturbation. The subsequent terms $\Theta_m^{(1)}$, $\Theta_m^{(2)}$, etc., describe higher-order (nonlinear) corrections. The frequency shift Ω_{mn} associated with the coupling of the m-th and n-th modes can then be written as:

$$\Omega_{mn} = \frac{d}{dt}(\Theta_m - \Theta_n). \tag{20}$$

This formulation establishes the connection between modal phase perturbations and observable frequency shifts in the interference pattern. This connection forms the theoretical basis for estimating the characteristics of oceanic inhomogeneities through modal interaction analysis.

$$\Omega_{mn}(r, \alpha) = -\frac{\Theta_{mn}(r, \alpha, f_0)}{G_{mn}}, \quad 0 \le r \le r_0, \tag{21}$$

where $(G_{mn})^{-1} = \left\{ r_0 \left[dh_{mn}(f_0)/d\omega \right] \right\}^{-1}$ is the frequency scale of field variability at distance r_0, determined by modal interference; f_0 is the frequency position of the observed interference maximum in the absence of ISW; and $\Theta_{mn} = \Theta_m - \Theta_n$ is the phase difference between the modes. Using the definition of the group velocity for the m-th mode, $v_{gm} = d\omega/dh_m$, the coefficient G_{mn} can be written as $G_{mn} = t_{mn}$, where $t_{mn} = t_m - t_n$ represents the time delay between pulses of modes m and n, with $t_m = r_0/v_{gm}$. Thus, Equation (21) shows that phase variations induced by environmental perturbations can be equivalently interpreted in terms of frequency shifts. In particular, the modal phase increment

Θ_{mn} can be expressed in terms of the frequency shift Ω_{mn} as $\Theta_{mn} = -t_{mn}\Omega_{mn}$. In other words, frequency shift measurements can serve as indirect phase measurements and can be used effectively in interferometric systems for diagnostic and monitoring purposes.

The solution to Equation (12) can be obtained using the integral method with a second-order approximation. For most practical applications, this approximation is accurate enough to study the influence of oceanic inhomogeneities.

3.3. ISW Propagates Along the Source–Receiver Path. Case $\alpha = 0$.

This case corresponds to an angle $\alpha = 0$ (see Figure 5). Substituting the mode amplitudes M_m and M_n with their initial values M_{m0} and M_{n0} into the right-hand side of the Equation (12) and integrating, we obtain

$$M_m(r) = M_{m0} + \mathrm{i}\Big[M_{m0}\int_0^r \mu_{mm}(r')\,dr' + M_{n0}\int_0^r \mu_{mn}(r')\,\exp(\mathrm{i}h_{mn}r')\,dr'\Big]. \tag{22}$$

Performing the second iteration, we obtain:

$$\begin{aligned} M_m(r) = M_{m0} + \Big\{ &- \Big[M_{m0}\int_0^r\int_0^s \mu_{mm}(s)\mu_{mm}(\sigma)\,d\sigma\,ds \\ &+ M_{n0}\int_0^r\int_0^s \mu_{mn}(s)\mu_{mn}(\sigma)\,\mathrm{e}^{\mathrm{i}h_{mn}\sigma}\,d\sigma\,ds\Big] \\ &+ M_{n0}\int_0^r\int_0^s \mu_{mn}(s)e^{\mathrm{i}h_{mn}s}\mu_{mn}(\sigma)\,\mathrm{e}^{\mathrm{i}h_{mn}\sigma}\,d\sigma\,ds \\ &+ M_{m0}\int_0^r\int_0^s \mu_{mm}(s)\mu_{mm}(\sigma)\,\mathrm{e}^{\mathrm{i}h_{mn}\sigma}\,d\sigma\,ds \\ &+ \mathrm{i}\Big[M_{m0}\int_0^r \mu_{mm}(s)\,ds + M_{n0}\int_0^r \mu_{mn}(s)\,\mathrm{e}^{\mathrm{i}h_{mn}s}\,ds\Big]\Big\}. \end{aligned} \tag{23}$$

As can be seen, the first-order solution compared with the second-order one underestimates the increment of the complex amplitude δM_m extracted in Equation (22) and Equation (23) from the expressions within the curly brackets. To determine the complex amplitude, it is sufficient to substitute lower indices $m \to n$ in Equations (22) and (23).

Using Equations (18) and (23), we can isolate the phase increment Θ_m and substitute it into Equation (19), by restricting ourselves to the first two terms. Using Equations (5), (15), and (16) the integration yields an expression for the phase increment Θ_m. Similarly, we can obtain the phase increment Θ_n. Then, accurate to quadratic terms, the expression for the phase difference Θ_{mn}, when transformed to the temporal dependence $t = r/v$, can be written as

$$\begin{aligned} \Theta_{mn}(t) &= \bar{\Theta}_{mn} + \hat{\Theta}_{mn}(t), \quad t_1 \le t \le t_2, \\ t_1 &= \frac{2v}{L}, \qquad t_2 = \frac{r_0 - 2v}{L}, \end{aligned} \tag{24}$$

where $\bar{\Theta}_{mn}$ is the stationary component of the phase difference, $\hat{\Theta}_{mn}(t)$ represents the oscillating component of the phase difference.

The stationary component of the phase difference $\bar{\Theta}_{mn}$ is defined by the following expression:

$$\bar{\Theta}_{mn} = J_1 + J_2 + J_3 + J_4. \tag{25}$$

In this context, the quantities J_i represent the following constant:

$$\begin{aligned}
J_1 &= 2AL(q_{mn} - q_{nn}),\\
J_2 &= 4(AL)^3(q_{mn}^3 - q_{nn}^3),\\
J_3 &= 2(AL)^3 q_{mn}^2 \frac{\sin^2(\varphi_{mn})}{\varphi_{mn}^2}\,(q_{mn} - q_{nn}),\\
J_4 &= 2(AL)^3 q_{mn}^2 \frac{\sin^2(\varphi_{mn})}{\varphi_{mn}^2}\left\{(q_{mm} + q_{nn})\left[\left(\frac{M_{n0}}{M_{m0}}\right)^2 - \left(\frac{M_{m0}}{M_{n0}}\right)^2\right]\right\}.
\end{aligned} \tag{26}$$

The oscillating component of the phase difference $\hat{\Theta}_{mn}(t)$ is defined by the expression:

$$\begin{aligned}
\hat{\Theta}_{mn}(t) = {} & I_1 \cos(\omega_{mn}t + \varphi_{mn}) + I_2 \sin(\omega_{mn}t)\\
& + I_3 \sin(\omega_{mn}t + \varphi_{mn}) + I_4 \sin(\omega_{mn}t + 2\varphi_{mn})\\
& + I_5 \sin(2\omega_{mn}t + \varphi_{mn}) + I_6 \sin(2\omega_{mn}t + 2\varphi_{mn})\\
& + I_7 \sin(2\omega_{mn}t + 3\varphi_{mn}) + I_8 \sin(3\omega_{mn}t + 2\varphi_{mn})\\
& + I_9 \sin(3\omega_{mn}t + 3\varphi_{mn}).
\end{aligned} \tag{27}$$

Here, the quantities I_i denote the following constants:

$$\begin{aligned}
I_1 &= 2ALq_{mn}\frac{\sin(\varphi_{mn})}{\varphi_{mn}}\left[\left(\frac{M_{n0}}{M_{m0}} - \frac{M_{m0}}{M_{n0}}\right) + 2(AL)^2\left(q_{mm}^2\frac{M_{n0}}{M_{m0}} - q_{nn}^2\frac{M_{m0}}{M_{n0}}\right)\right.\\
&\quad \left. + (ALq_{mn})^2\frac{\sin^2(\varphi_{mn})}{\varphi_{mn}^2}\left(\frac{M_{n0}}{M_{m0}} - \frac{M_{m0}}{M_{n0}}\right)\right],\\
I_2 &= \frac{A^3L^3q_{mn}}{\varphi_{mn}}\left[q_{mn}^2\frac{\sin^2(\varphi_{mn})}{\varphi_{mn}^2}\left(\frac{M_{n0}}{M_{m0}} - \frac{M_{m0}}{M_{n0}}\right) - 4\left(q_{mm}^2\frac{M_{n0}}{M_{m0}} - q_{nn}^2\frac{M_{m0}}{M_{n0}}\right)\right],\\
I_3 &= \frac{A^3L^3q_{mn}}{\varphi_{mn}}\frac{\sin(\varphi_{mn})}{\varphi_{mn}}\left[4\left(q_{mm}^2\frac{M_{n0}}{M_{m0}} - q_{nn}^2\frac{M_{m0}}{M_{n0}}\right)\right.\\
&\quad \left. + \left(q_{mn}^2\frac{\sin(2\varphi_{mn})}{2\varphi_{mn}} - 4q_{mm}q_{nn}\right)\left(\frac{M_{n0}}{M_{m0}} - \frac{M_{m0}}{M_{n0}}\right)\right],\\
I_4 &= \frac{4A^3L^3q_{mm}q_{nn}q_{mn}}{\varphi_{mn}}\left(\frac{M_{n0}}{M_{m0}} - \frac{M_{m0}}{M_{n0}}\right),\\
I_5 &= -\frac{2A^3L^3q_{mn}^2}{\varphi_{mn}}\frac{\sin(\varphi_{mn})}{\varphi_{mn}}\left\{(q_{mm} - q_{nn}) + \left[q_{mm}\left(\frac{M_{n0}}{M_{m0}}\right)^2 - q_{nn}\left(\frac{M_{m0}}{M_{n0}}\right)^2\right]\right\},\\
I_6 &= \frac{2A^3L^3q_{mn}^2}{\varphi_{mn}}(q_{mm} - q_{nn})\left\{\frac{\sin(2\varphi_{mn})}{2\varphi_{mn}} + \frac{\sin^2(\varphi_{mn})}{\varphi_{mn}^2}\left[\left(\frac{M_{n0}}{M_{m0}}\right)^2 + \left(\frac{M_{m0}}{M_{n0}}\right)^2\right]\right\},\\
I_7 &= \frac{2A^3L^3q_{mn}^2}{\varphi_{mn}}\frac{\sin(\varphi_{mn})}{\varphi_{mn}}\left[q_{nn}\left(\frac{M_{n0}}{M_{m0}}\right)^2 - q_{mm}\left(\frac{M_{m0}}{M_{n0}}\right)^2\right],\\
I_8 &= \frac{A^3L^3q_{mn}^3}{\varphi_{mn}}\frac{\sin^2(\varphi_{mn})}{\varphi_{mn}^2}\left(\frac{M_{n0}}{M_{m0}} - \frac{M_{m0}}{M_{n0}}\right),\\
I_9 &= \frac{A^3L^3q_{mn}^3}{\varphi_{mn}}\frac{\sin(\varphi_{mn})}{\varphi_{mn}}\frac{\sin(2\varphi_{mn})}{2\varphi_{mn}}\left(\frac{M_{n0}}{M_{m0}} - \frac{M_{m0}}{M_{n0}}\right).
\end{aligned} \tag{28}$$

Here, $\varphi_{mn} = |h_{mn}|L$ is the oscillation phase, $\omega_{mn} = 2\pi\nu_{mn}$, and $\nu_{mn} = |h_{mn}|v/2\pi$ is the first harmonic of the oscillations of the interacting m-th and n-th modes. Using the definition of the spatial beat period of the interacting modes $\rho_{mn} = 2\pi/|h_{mn}|$, the frequency ν_{mn} can be written as $\nu_{mn} = v/\rho_{mn}$. Thus, the value $1/\nu_{mn}$ can thus be interpreted as the characteristic displacement time of the interference pattern ρ_{mn}/v. Variations in the velocity of the inhomogeneous region lead to proportional variations in the oscillation frequency ν_{mn} without affecting the amplitude.

In Equation (25), the first term defines the stationary frequency shift in the independent mode approximation of the (the linear term in Equation (19)), while the remaining two terms arise due to mode interaction (the quadratic terms in Equation (19)). The resulting oscillations of the phase difference $\hat{\Theta}_{mn}(t)$ include harmonics with frequencies ω_{mn}, $2\omega_{mn}$, and $3\omega_{mn}$. As in the case of independent normal modes, the interaction of modes leads to changes in the mean values of the phase difference and frequency shifts.

The phase difference $\hat{\Theta}$ between the interfering modes leads to the appearance of harmonics of the phase difference $\hat{\Theta}$. These two mechanisms differ qualitatively in that the mean phase difference is mainly determined by the parameters q_{mn} and q_{nn}, which are associated with corrections to the unperturbed values of the propagation constants. The amplitude of the oscillatory phase component is defined by the parameters q_{mn}, h_{mn}, and the interaction coefficient μ_{mn} which governs mode coupling.

The expressions for the coefficients J_j (Equation (26)) and I_i (Equation (28)) were obtained under the approximation $|\Theta_{mn}| < 1$. To satisfy this condition, it is necessary to assume that the mode amplitudes M_{m0} and M_{n0} are of the same order, i.e., $M_{m0} \sim M_{n0}$. If one of the modes is weakly excited (for example, $M_{m0} \gg M_{n0}$), then, as $M_{n0} \to 0$, the ratio M_{m0}/M_{n0} increases indefinitely, and the small-parameter approximation is violated. In this case, the system (Equation (12)) must be solved using the initial condition $M_{n0} = 0$.

According to Equations (21) and (24), the frequency shift can be written as

$$\Omega(t) = -\frac{1}{G_{mn}}(\bar{\Theta}_{mn} + \hat{\Theta}_{mn}) = \bar{\Omega} + \hat{\Omega}(t). \tag{29}$$

As can be seen from Equations (24), (26), and (29), this formulation does not describe the frequency shift modulation of observed in numerical experiments (see Section 4). This discrepancy arises from the approximate nature of Equation (21), which is based on the Taylor expansion of the propagation constants h_m around their unperturbed values h_{m0}. For the reference value f_0, which corresponds to the position of the maximum of the field in the absence of perturbation, the linear term of the expansion is sufficient for stationary frequency shift patterns. However, for nonstationary patterns, where the position of $\Omega(t)$ varies over time, the interference of waves with closely spaced frequencies must be considered. In this case, small variations in the propagation constants produce beatings that manifest as frequency modulation.

Now, let us consider the spectrum of the interferogram of frequency shifts, which qualitatively represents the essence of the phenomenon. As shown by numerical simulations (see Section 4), the amplitudes of the spectral components $p\nu_{mn}$, (for $p = 1, 2, 3$), decrease with increasing harmonic number p, and higher harmonics have significantly smaller spectral amplitudes. The amplitude of the frequency shift at the frequency $\nu_{mn} = 0$ is determined by the stationary component $\bar{\Omega}_{mn}$. In this case, the spectral component $3\nu_{mn}$ is negligible small, so its amplitude is not visible in the figures. Therefore, we restrict our analysis to the stationary term and the first harmonic ω_{mn} of the frequency shifts (Equation (29)).

Table 3. Parameters of an unperturbed waveguide

Parameter	**Value**
h_{12}, $\times 10^{-3}\,\mathrm{m}^{-1}$	7.590
M_{01}	0.1352
M_{02}	0.1577
q_{11}, $\times 10^{-4}\,\mathrm{m}^{-2}$	1.2860
q_{22}, $\times 10^{-4}\,\mathrm{m}^{-2}$	2.8095
q_{12}, $\times 10^{-4}\,\mathrm{m}^{-2}$	2.0070
G_{12}, s	0.3391

For the unperturbed waveguide model, the parameters that define the values of the coefficients J_i, and I_i, as well as the magnitude G_{12} are given in Table 3. Note that the propagation of the first ($m = 1$) and second ($n = 2$) modes was modeled. Now, if we apply the inverse Fourier transform:

$$\hat{\Omega}(\omega) = \frac{1}{2\pi} \int_{-\infty}^{\infty} \Omega(t)\, \exp(-i\omega t)\, dt, \tag{30}$$

then, neglecting the edge effects associated with the incomplete entry and exit of the soliton from the track, the amplitudes of the spectral components at frequencies $\omega = 0$ and $\omega = \omega_{mn}$ can be easily found as

$$\hat{\Omega}(0) = \frac{T}{2\pi G_{mn}} J, \qquad J = J_1 + J_2, \tag{31}$$

and

$$\hat{\Omega}(\omega = \omega_{mn}) = \frac{T}{4\pi G_{mn}}\, I, \tag{32}$$

$$I = \sqrt{I_1^2 + I_2^2 + I_3^2 + I_4^2 + 2I_3(I_2 + I_4)\cos(\varphi_{mn}) + 2I_1(I_4 - I_2)\sin(\varphi_{mn}) + 2I_2 I_4 \cos(2\varphi_{mn})}.$$

Here, I denotes the amplitude of the harmonic of the phase difference; $T = r_0/v$ is the soliton passage time along the acoustic track. Note that the Equation (31) remains valid when edge effects are considered, if the pulse is approximated by a trapezoidal shape. In this case, the broadening width of the spectral lines at the level of 0.7 of the maximum amplitude can be estimated as

$$\delta\nu = 0.9\, \frac{v}{r_0}, \tag{33}$$

that is, to within a factor of 0.9, it is inversely proportional to the travel time T and independent of the interacting mode number. Note that the expressions for the oscillation frequencies ν_{mn} and the spectral linewidth $\Delta\nu$ were previously obtained based on numerical experiments.

3.4. ISW Propagates at an Angle to the Source-Receiver Path. Case $\alpha \neq 0$.

Consider the propagation of an ISW with the source-receiver path at an angle of α, where $0 < \alpha < \pi/2$. As can be seen from the geometry of the problem shown in Figure 5, the problem reduces to the case of motion along the path with an angle of $\alpha = 0$, if one introduces the effective half-width $L(\alpha)$, the ISW velocity $v(\alpha)$, and the ISW traversal time along the source-receiver path $T(\alpha)$:

$$L(\alpha) = \frac{L}{\cos(\alpha)}, \qquad v(\alpha) = \frac{v}{\cos(\alpha)}, \qquad T(\alpha) = T\cos(\alpha). \tag{34}$$

Here, L, v, and T denote the corresponding quantities for $\alpha = 0$. Equations (24)–(33) remain valid in this case if the appropriate substitutions are made. However, as the angle approaches $\pi/2$, the coupled modes approximation becomes less effective. In this case, significant horizontal refraction effects caused by ISWs crossing the source-receiver path must be considered.

According to Equation (25) and (26), an increase in α leads to growth in the mean frequency shift $\bar{\Omega}$ and the adiabatic frequency shift Ω_{ad} (calculated without mode coupling), as well as a decrease in the amplitude of the oscillatory component $\hat{\Omega}(t)$. The frequency $\nu_{mn}(\alpha)$ and the width $\delta\nu(\alpha)$ of the spectral lines are given by

$$\nu_{mn}(\alpha) = \frac{\nu_{mn}}{\cos(\alpha)}, \qquad \delta\nu(\alpha) = \frac{\delta\nu}{\cos(\alpha)}. \tag{35}$$

Thus, an increase in α leads to a proportional increase by a factor of $(1/\cos(\alpha))$. At the same time, the ratio of the linewidth $\delta\nu(\alpha)$, cf. Equation (33), to the oscillation frequency $\nu_{mn}(\alpha)$ can be written as

$$\frac{\delta\nu(\alpha)}{\nu_{mn}(\alpha)} = 0.9 \cdot 2\pi \left(|h_{mn}| r_0\right)^{-1}, \tag{36}$$

which is independent of the perturbation. Furthermore, the dependence of the corresponding values on the angle α will be omitted unless it causes ambiguity.

4. Numerical Simulation Results

This section presents the results of numerical simulations of frequency-shift dynamics induced by ISWs. These simulations were performed using the parameter set summarized in Table 2. Figure 3 shows the unperturbed sound-speed profile as a function of depth. The bottom properties were specified by the density ratio of the bottom sediments to water, $\rho_b/\rho = 1.8$, and the complex refractive index $n_b = 0.82\,(1 + \mathrm{i}\,0.01)$. In the 90–120 Hz frequency band, modal groups with nearly equal amplitudes were considered, using a spectral resolution of $\delta f = 0.2\,\mathrm{Hz}$. The acoustic source and the receiver were both placed at a depth of $z_0 = 30\,\mathrm{m}$, and the horizontal propagation range was set to $r_0 = 10\,\mathrm{km}$. The soliton was represented by a squared hyperbolic secant pulse with an amplitude of $A = 15\,\mathrm{m}$, a half-width of $L = 100\,\mathrm{m}$, and a propagation velocity of $v = 1\,\mathrm{m/s}$. Particular attention was given to the coupling between the first and second acoustic modes ($m = 1$, $n = 2$), since this modal pair demonstrates the strongest interaction.

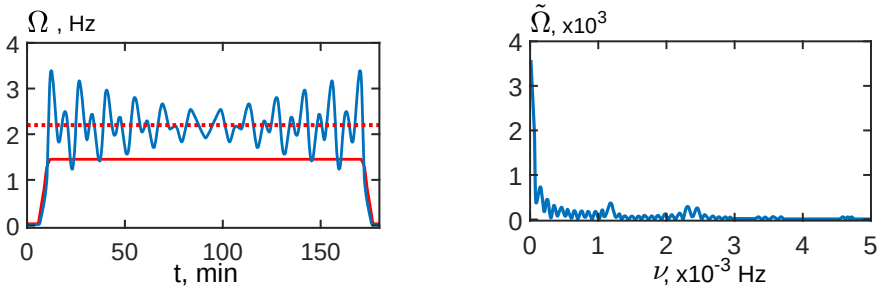

(**a**) (**b**)

Figure 8. (a) Frequency shift $\Omega(t)$ due to ISW. Red dotted line – mean value of $\Omega(t)$. Red solid line – $\Omega(t)$ without mode coupling. **(b)** Spectrum $\tilde{\Omega}(\nu)$ of frequency shifts $\Omega(t)$. ISW parameters: $A = 15\,\mathrm{m}$, $L = 100\,\mathrm{m}$, $v = 1\,\mathrm{m/s}$, $\alpha = 0^\circ$. ISW is modeled by a squared hyperbolic secant (KdV-solution) shape. Acoustic attenuation due to the bottom is present: $\varkappa \neq 0$.

Figure 8 illustrates the temporal and spectral manifestations of ISW-induced frequency shifts when acoustic attenuation associated with bottom interaction is considered. The ISW is modeled using a squared hyperbolic secant (KdV-solution) shape. Panel (a) of Figure 8 shows that the time dependence of the frequency shift $\Omega(t)$ retains the same general structure as in the lossless case. During the ISW influence interval, the frequency shifts dependence consists of a nearly stationary mean component with superimposed oscillations. Outside this interval, the shift rapidly approaches zero. The red solid line represents the contribution without mode coupling and defines the slowly varying background level. The blue curve shows that mode coupling produces an additional oscillatory modulation around this baseline. The red dashed line shows the mean value of $\Omega(t)$, which remains close to the central level of the oscillatory response throughout the disturbed interval. Figure 8(b) provides an additional interpretation of these results through its spectral representation. The spectrum $\tilde{\Omega}(\nu)$ is concentrated primarily in the low-frequency range. It has a dominant peak near zero frequency and a sequence of weaker harmonics extending toward higher frequencies ν.

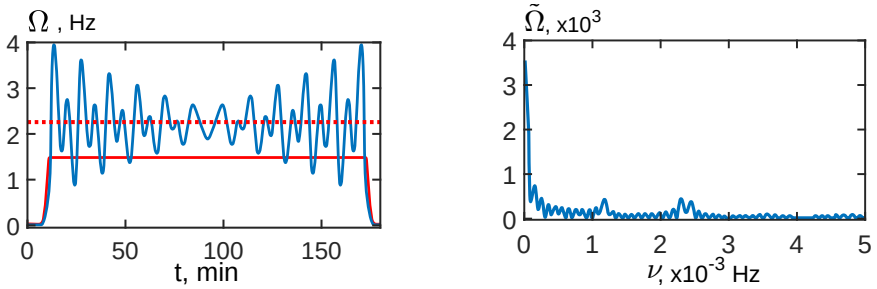

Figure 9. (a) Frequency shift $\Omega(t)$ due to ISW. Red dotted line – mean value of $\Omega(t)$. Red solid line – $\Omega(t)$ without mode coupling. **(b)** Spectrum $\tilde{\Omega}(\nu)$ of frequency shifts $\Omega(t)$. ISW parameters: $A = 15\,\text{m}$, $L = 100\,\text{m}$, $v = 1\,\text{m/s}$, $\alpha = 0°$. ISW is modeled by an approximate rectangular shape. Acoustic attenuation due to the bottom is present: $\varkappa \neq 0$.

Figure 9 shows the temporal evolution and spectral content of the ISW-induced frequency shift $\Omega(t)$ for the case in which the internal wave is represented by an approximate rectangular profile and acoustic attenuation due to bottom interaction is included. Panel (a) of Figure 9 shows that the frequency shift remains localized within the time interval during which the inhomogeneity intersects the source-receiver path. During this time, the signal consists of a nearly steady background component and a superimposed oscillatory contribution. Outside of this interaction interval, $\Omega(t)$ rapidly drops to values close to zero, indicating that the ISW's perturbing effect on the interference structure vanishes as the wave moves away from the acoustic path. The spectral behavior shown in Figure 9(b) is consistent with the time-domain picture. The spectrum $\tilde{\Omega}(\nu)$ is concentrated primarily in the low-frequency range. There is a dominant contribution located near zero frequency and a set of weaker secondary maxima at higher frequencies ν. This structure reflects the coexistence of two components in $\Omega(t)$: a non-zero average level, which produces the strong low-frequency part of the spectrum, and an oscillatory modulation, which gives rise to additional spectral peaks. Therefore, the spectrum confirms that the ISW-induced frequency shift is mainly governed by slow temporal variability, while the finer oscillatory structure contributes weaker, yet still well-resolved harmonic content.

An important conclusion that can be drawn from Figure 9 is that the approximate rectangular representation of the ISW retains the same main temporal and spectral signatures as the squared hyperbolic secant (KdV-solution) shape. Replacing the soliton profile has little effect on the mean frequency shifts and does not alter the positions of the spectral lines. However, it leads to an increase in the amplitudes of the spectral components. For example, at the frequency $\nu = 1.174 \times 10^{-3}\,\text{Hz}$, the oscillation amplitude $\tilde{\Omega}$ is equal to 341.94 for the sech^2 ISW and 416.38 for the rectangular ISW. Thus, changing the ISW shape mainly affects the spectral components amplitudes, while leaving the overall spectral structure nearly unchanged. Not only is the stationary interference pattern of frequency shifts observed, as in the case of independent modes, but also a time-dependent process associated with variations in the path difference of modes propagating from the inhomogeneity to the receiver. Additionally, the constant frequency shifts $\bar{\Omega}$ differ for coupled and independent modes.

Figure 10 shows the temporal evolution and spectrum of the ISW-induced frequency shift $\Omega(t)$ for an approximate rectangular wave profile in the absence of bottom attenuation. As seen in Panel (a) of Figure 10, the frequency shift is localized within the interaction interval between the inhomogeneity and the source-receiver path. During this interval, $\Omega(t)$ consists of a nearly constant mean level and an oscillatory component caused by mode coupling. Outside this interval, it rapidly approaches zero. The corresponding spectrum $\tilde{\Omega}(\nu)$, shown in Panel (b) of Figure 10, is concentrated mainly in the low-frequency range and has a dominant peak near zero frequency and several weaker secondary maxima.

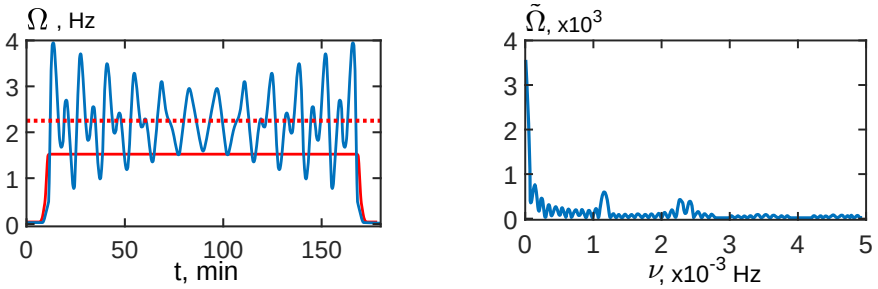

Figure 10. **(a)** Frequency shift $\Omega(t)$ due to ISW. Red dotted line – mean value of $\Omega(t)$. Red solid line – $\Omega(t)$ without mode coupling. **(b)** Spectrum $\tilde{\Omega}(\nu)$ of frequency shifts $\Omega(t)$. ISW parameters: $A = 15$ m, $L = 100$ m, $v = 1$ m/s, $\alpha = 0°$. ISW is modeled by an approximate rectangular shape. Acoustic attenuation due to bottom is absent: $\varkappa = 0$.

Comparing this figure with Figure 9, which includes bottom attenuation, shows that excluding bottom absorption does not substantially change the temporal behavior or the spectral structure of the frequency shifts. The mean level, the oscillation pattern, and the positions of the main spectral peaks remain nearly the same. This suggests that the influence of bottom attenuation weakly influences the frequency shifts and does not affect the main features of the ISW-induced response. For example, at $\nu = 1.174 \times 10^{-3}$ Hz, the mean frequency shift without attenuation is $\tilde{\Omega} = 577.35$, whereas with attenuation included, it is $\tilde{\Omega} = 341.94$. This demonstrates that attenuation primarily affects the magnitude of the spectral components but does not influence the frequency shift distribution pattern itself.

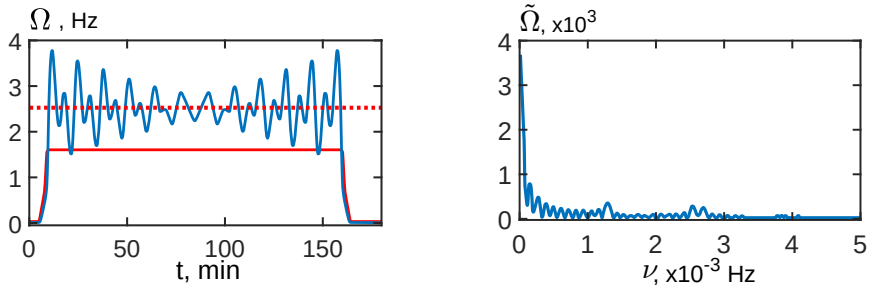

Figure 11. **(a)** Frequency shift $\Omega(t)$ due to ISW. Red dotted line – mean value of $\Omega(t)$. Red solid line – $\Omega(t)$ without mode coupling. **(b)** Spectrum $\tilde{\Omega}(\nu)$ of frequency shifts $\Omega(t)$. ISW parameters: $A = 15$ m, $L = 100$ m, $v = 1$ m/s, $\alpha = 25°$. ISW is modeled by a squared hyperbolic secant (KdV-solution) shape. Acoustic attenuation due to the bottom is present: $\varkappa \neq 0$.

Figures 11–13 illustrate how the temporal and spectral characteristics of the ISW-induced frequency shift $\Omega(t)$ depend on the angle α between the wave propagation direction and the acoustic track. In all three cases include acoustic attenuation due to bottom interaction, and the ISW is modeled by the sech^2-type KdV profile. A common feature of all panels is that the frequency shift remains localized within the time interval during which the inhomogeneity affects the source-receiver path. Outside this interval $\Omega(t)$ rapidly tends to zero. The corresponding spectra $\tilde{\Omega}(\nu)$ are dominated by low-frequency components, reflecting the finite duration and relatively slow temporal modulation of the ISW-induced perturbation. Comparing of panels (a) in Figures 11–13 reveals a clear systematic influence of the angle α. As α increases from 25° to 50° and then to 75°, the duration of the disturbed interval decreases noticeably, while the mean level of the frequency shift increases. At $\alpha = 25°$, the signal extends over the longest time interval and exhibits a well-developed oscillatory structure around a moderate mean level. At $\alpha = 50°$, the interaction interval becomes shorter and the average value of $\Omega(t)$ grows; however, the oscillations remain clearly visible. At $\alpha = 75°$, the response is strongly

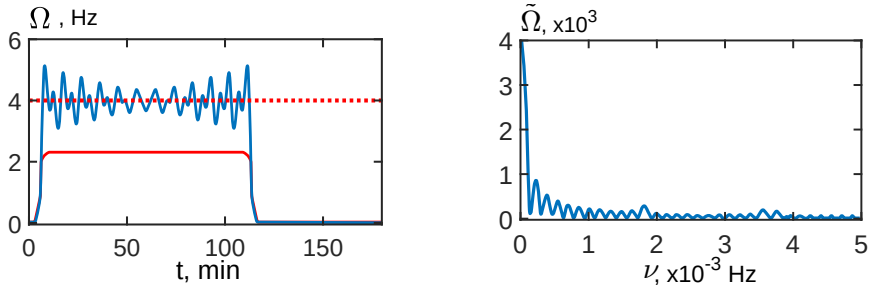

(**a**) (**b**)

Figure 12. **(a)** Frequency shift $\Omega(t)$ due to ISW. Red dotted line – mean value of $\Omega(t)$. Red solid line – $\Omega(t)$ without mode coupling. **(b)** Spectrum $\tilde{\Omega}(\nu)$ of frequency shifts $\Omega(t)$. ISW parameters: $A = 15\,\text{m}$, $L = 100\,\text{m}$, $v = 1\,\text{m/s}$, $\alpha = 50°$. ISW is modeled by a squared hyperbolic secant (KdV-solution) shape. Acoustic attenuation due to the bottom is present: $\varkappa \neq 0$.

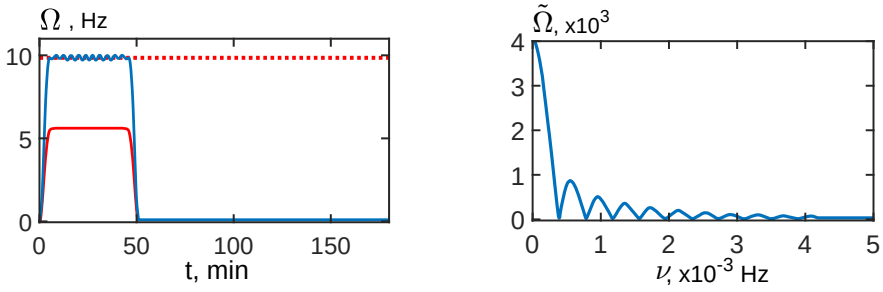

(**a**) (**b**)

Figure 13. **(a)** Frequency shift $\Omega(t)$ due to ISW. Red dotted line – mean value of $\Omega(t)$. Red solid line – $\Omega(t)$ without mode coupling. **(b)** Spectrum $\tilde{\Omega}(\nu)$ of frequency shifts $\Omega(t)$. ISW parameters: $A = 15\,\text{m}$, $L = 100\,\text{m}$, $v = 1\,\text{m/s}$, $\alpha = 75°$. ISW is modeled by a squared hyperbolic secant (KdV-solution) shape. Acoustic attenuation due to the bottom is present: $\varkappa \neq 0$.

compressed in time and is characterized by a much larger mean frequency shift, while the oscillatory modulation is relatively weak compared to the overall level of the signal. The same tendency is evident in the spectral domain. For $\alpha = 25°$, the spectrum contains a pronounced low-frequency peak, as well as a relatively rich set of secondary maxima associated with the oscillatory structure of $\Omega(t)$. As the angle increases to 50°, the spectrum remains dominated by low frequencies, though the secondary components become less significant relative to the main contribution. In the case $\alpha = 75°$, the spectral energy is concentrated even more strongly in the lowest-frequency range, and the fine harmonic structure becomes much less pronounced. Thus, as α increases, the spectral pattern gradually simplifies, which is consistent with the reduced relative importance of oscillatory modulation in the time domain.

Overall, the comparative analysis of Figures 11–13 shows that the angle α is one of the key parameters controlling the ISW-induced frequency shifts. An increase in this angle yields larger mean values of $\Omega(t)$, shorter interaction times, and a stronger spectral energy concentration near zero frequency. At the same time, the contribution of mode-coupling-induced oscillations becomes less pronounced in relative terms. Therefore, the geometry of ISW propagation relative to the acoustic path significantly impacts the temporal signature and spectral content of the observed frequency-shift response.

Table 4. Frequency Shifts Parameters. Case $\alpha = 0°$.

Parameter	Theory	Simulation
Ω_{ad}, Hz	1.348	1.452
$\bar{\Omega}$, Hz	2.075	2.188
ν_{12}, $\times 10^{-4}$ Hz	1.209	1.174
$\delta\nu$, $\times 10^{-4}$ Hz	0.899	0.909
Spectral amplitude at the frequency ν_{12}	605.33	341.94

Table 5. Frequency Shifts Parameters. Case $\alpha = 25°$.

Parameter	Theory	Simulation
Ω_{ad}, Hz	1.487	1.602
$\bar{\Omega}$, Hz	2.468	2.524
ν_{12}, $\times 10^{-4}$ Hz	1.333	1.295
$\delta\nu$, $\times 10^{-4}$ Hz	0.992	1.018
Spectral amplitude at the frequency ν_{12}	642.65	331.22

Table 6. Frequency Shifts Parameters. Case $\alpha = 50°$.

Parameter	Theory	Simulation
Ω_{ad}, Hz	2.097	2.286
$\bar{\Omega}$, Hz	4.904	3.981
ν_{12}, $\times 10^{-4}$ Hz	1.880	1.810
$\delta\nu$, $\times 10^{-4}$ Hz	1.556	1.363
Spectral amplitude at the frequency ν_{12}	728.18	264.19

Table 7. Frequency Shifts Parameters. Case $\alpha = 75°$.

Parameter	Theory	Simulation
Ω_{ad}, Hz	5.207	5.531
$\bar{\Omega}$, Hz	51.178	9.737
ν_{12}, $\times 10^{-4}$ Hz	—	—
$\delta\nu$, $\times 10^{-4}$ Hz	—	—
Spectral amplitude at the frequency ν_{12}	—	—

The frequency-shift modeling results for $\alpha = 0°, 25°, 50°$, and $75°$ are summarized in the following tables: Table 4 corresponds to Figure 8 ($\alpha = 0°$); Table 5 corresponds to Figure 11 ($\alpha = 25°$); Table 6 corresponds to Figure 12 ($\alpha = 50°$); Table 7 corresponds to Figure 13 ($\alpha = 75°$). An increase in α leads to an increase in the stationary component $\bar{\Theta}_{mn}$, a decrease in the amplitude of the oscillatory phase component, and an increase in the adiabatic frequency shift ν_{mn}, which agrees qualitatively with theoretical expectations. For $\alpha = 75°$, oscillations of the frequency shifts practically vanish, and the corresponding spectral lines are not registered against the stationary spectrum background. At the same time, the difference between the adiabatic and stationary frequency shifts Ω_{ad} and $\bar{\Omega}$ increases. Interference between the modes becomes noticeable for angles greater than $\alpha > 50°$, which is related to the coupling of two terms in Equation (19) that were used to construct the numerical model. To reduce discrepancies arising as the angle α increases, higher-order approximations must be considered, which complicates solving the inverse problem. However, this refinement has limited physical significance since the proposed theory does not consider horizontal mode refraction, which becomes noticeable for angles $\alpha > 70°$. Therefore, it can be concluded that Equation (19) is applicable only to angles $\alpha \lesssim 50°$.

5. Internal Soliton Wave Parameters Estimation

Although this possibility had previously been questioned, theoretical analysis suggests that the inverse problem can be addressed using information about the frequency shifts of coupled normal modes. To clarify, we consider a numerical experiment schematically illustrated in Figure 14. Two acoustic propagation paths originate from a common source S and terminate at receivers Q_1 ($\alpha_1 = 20°$) and Q_2 ($\alpha_2 = 40°$), which are positioned so that the angle between the paths is $\varphi = 20°$. The length of each path is $r_0 = 10$ km. We assume that the characteristics of the unperturbed acoustic waveguide are known (see Table 2).

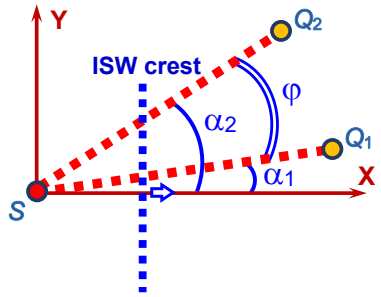

Figure 14. Geometry of the problem: S - source; Q_1 - first receiver; Q_2 - second receiver; red dashed lines - $S-Q_1$ and $S-Q_2$ paths; blue dashed line - ISW crest; blue arrow - ISW velocity vector $\mathbf{v}$; $\alpha_1 = 20°$ angle between $S-Q_1$ path and X-axis; $\alpha_2 = 40°$ angle between $S-Q_2$ path and X-axis; φ angle between $S-Q_1$ and $S-Q_2$ paths.

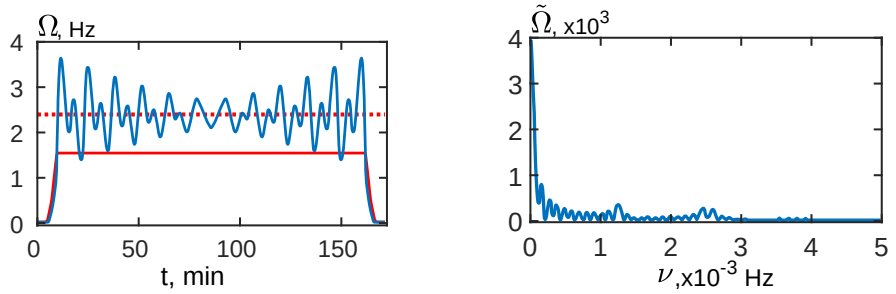

(**a**) (**b**)

Figure 15. **(a)** Frequency shift $\Omega(t)$ due to ISW. Red dotted line – mean value of $\Omega(t)$. Red solid line – $\Omega(t)$ without mode coupling. **(b)** Spectrum $\tilde{\Omega}(\nu)$ of frequency shifts $\Omega(t)$. ISW parameters: $A = 15$ m, $L = 100$ m, $v = 1$ m/s, $\alpha_1 = 20°$. ISW is modeled by a squared hyperbolic secant (KdV-solution) shape. Acoustic attenuation due to bottom is present: $\varkappa \neq 0$. Results corresponds to $S-Q_1$ path.

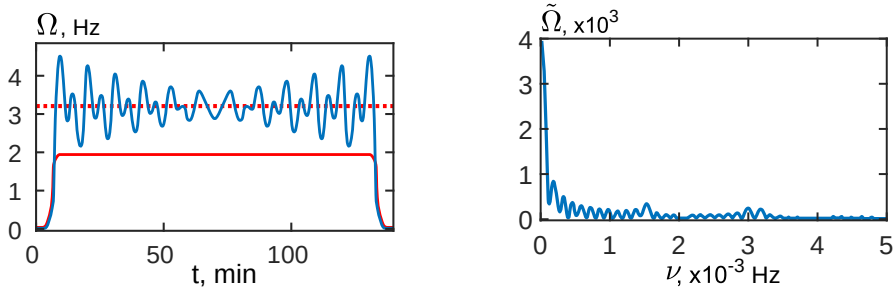

(**a**) (**b**)

Figure 16. **(a)** Frequency shift $\Omega(t)$ due to ISW. Red dotted line – mean value of $\Omega(t)$. Red solid line – $\Omega(t)$ without mode coupling. **(b)** Spectrum $\tilde{\Omega}(\nu)$ of frequency shifts $\Omega(t)$. ISW parameters: $A = 15$ m, $L = 100$ m, $v = 1$ m/s, $\alpha_2 = 40°$. ISW is modeled by a squared hyperbolic secant (KdV-solution) shape. Acoustic attenuation due to bottom is present: $\varkappa \neq 0$. Results corresponds to $S-Q_2$ path.

The ISW intersects both propagation paths at angles α_1 and α_2. The simulation uses the following soliton parameters: amplitude $A = 15\,\text{m}$, half-width $L = 100\,\text{m}$, propagation velocity $v = 1\,\text{m/s}$, and intersection angles $\alpha_1 = 20^\circ$ and $\alpha_2 = 40^\circ$. The goal is to determine the soliton parameters and its direction of motion based on the frequency shifts obtained numerically, which are presented in Figures 15 and 16 for the first and second paths, respectively.

Table 8. Frequency Shifts Parameters. First Path.

Parameter	First path
ν_{12}, Hz	1.5376×10^{-3}
$\delta\nu$, Hz	1.1724×10^{-4}
$\bar{\Omega}$, Hz	3.1910

Table 9. Frequency Shifts Parameters. Second Path.

Parameter	Second path
ν_{12}, Hz	1.2650×10^{-3}
$\delta\nu$, Hz	9.8152×10^{-5}
$\bar{\Omega}$, Hz	2.3959

The values of the frequency-shift parameters obtained in the numerical experiment are summarized in Table 8 and Table 9. The procedure used to reconstruct the soliton parameters is outlined below. By measuring the oscillation frequencies $\nu_{12}(\alpha_1)$ and $\nu_{12}(\alpha_2)$ along the two acoustic paths, and taking into account the geometric relation between the angles, $\alpha_2 = \beta + \alpha_1$, an equation for determining α_2 can be obtained:

$$\tan(\alpha_1) = \frac{\gamma\cos(\beta) - 1}{\gamma\sin(\beta)}, \tag{37}$$

where $\gamma = \nu_{12}(\alpha_2)/\nu_{12}(\alpha_1)$. Using Equation (19), the soliton's propagation velocity can be estimated from measurements of the soliton propagation direction and the spectral line width recorded on one of the acoustic paths. This estimate can be written as

$$\nu = 1.1\, r_0\, \delta\nu(\alpha_{1,2})\, \cos(\alpha_{1,2}). \tag{38}$$

According to the parameters listed in Table 3, the contributions of the terms J_3 and J_4 in Equation (26) are small and can be neglected when evaluating the constant component $\bar{\Theta}_{mn}$ defined in Equation (25). Therefore, determining the soliton pulse parameter AL from measurements of the mean frequency shift $\Omega(\alpha_{1,2})$ reduces to solving a cubic equation. The average frequency shift corresponding to the angles $\alpha_{1,2}$ can be written in the form:

$$\bar{\Omega}(\alpha_{1,2}) = -\frac{1}{G_{12}}\left[\frac{2AL}{\cos(\alpha_{1,2})}(q_{11} - q_{22}) + \frac{4(AL)^3}{\cos^3(\alpha_{1,2})}(q_{11}^3 - q_{22}^3)\right]. \tag{39}$$

The difference in the propagation constants $|h_{12}|$ of the unperturbed waveguide can be obtained from Equation (36) using the available measurement data. This approach accounts for potential discrepancies between the actual and assumed environmental parameters during the experiment.

Table 10. ISW Parameters Estimation

Parameter	Model values	First-path data	Second-path data
v, m/s	1	1.013	1.031
α_2, deg	20°	18°54′	18°54′
AL, m^2	1500	1447	1509
$\lvert h_{12}\rvert$, m^{-1}	7.590×10^{-3}	7.413×10^{-3}	7.284×10^{-3}

At the same time, the problem of separating the factors contained in the parameter AL remains unresolved. The results of reconstructing the soliton characteristics are summarized in Table 10. These data show that the estimates of the soliton parameters obtained from the two paths are consistent. The parameter values reconstructed using the two acoustic paths show good agreement, demonstrating the stability and consistency of the obtained estimates.

6. Conclusion

The results of the present study demonstrate that the proposed monitoring approach, which is based on analyzing frequency-shifted maxima of the acoustic field, can extend well beyond the conventional regime of independent normal modes. Combined theoretical analysis and numerical simulations show that the previously assumed restriction to weakly perturbed environments is not fundamental. Notably, the method remains applicable in the presence of intense internal waves, even when the acoustic field is significantly impacted by mode coupling. This finding is significant because it expands the range of inverse problems that can be solved using this approach to include the recovery of parameters related to weak and pronounced oceanic inhomogeneities.

An important consequence of these findings is that the proposed approach can reconstruct not only the characteristics of oceanic inhomogeneities, but also their spatial and temporal variability, in a statistically meaningful way. Thus, the method provides information directly relevant to practical ocean acoustic monitoring, where the medium is often highly variable and only partially understood. Furthermore, the results indicate that the approach can be used in near-real-time applications while maintaining an acceptable level of accuracy in solving the inverse problem. These results significantly increase the approach's practical value, suggesting that frequency-shift analysis can serve as an effective diagnostic tool for monitoring complex shallow-water environments under realistic conditions.

More broadly, this study advances our physical understanding of sound propagation in shallow-water waveguides with strong spatiotemporal variability. The results clearly demonstrate that mode coupling must be considered when interpreting frequency shifts in these environments. Rather, it must be considered an essential physical mechanism that governs the transformation of the acoustic field. From this standpoint, the proposed monitoring framework provides a consistent physical basis for analyzing acoustic fields in environments with both weak and strong inhomogeneities. Overall, the study confirms the method's robustness and diagnostic potential and highlights its promise for further development in inverse problems and adaptive ocean acoustic monitoring.

Author Contributions: Supervision and project administration, M.E. and S.P.; conceptualization and methodology, V.K. and S.P.; software, S.T. and A.P.; validation, M.E. and V.K.; formal analysis, M.E. and S.P.; writing – original draft preparation, M.E. and S.P.; writing – review and editing, M.E. and S.P.; All authors have read and agreed to the published version of the manuscript.

Funding: This work was supported in part by the Ministry of Education and Science of the Russian Federation through Project No. FZGU-2026-0008. The numerical simulation of the frequency shifts was supported by a grant from the Russian Science Foundation № 23-61-10024, https://rscf.ru/project/23-61-10024/ (accessed on 23 March 2026).

Data Availability Statement: The original data used in the study are openly available. The waveguide model used in the simulation is based on parameters from the SWARM'95 experiments [39,40].

Conflicts of Interest: The authors declare no conflicts of interest.

Abbreviations

The following abbreviations are used in this manuscript:

ISP	interferometric signal processing;
HSP	holographic signal processing;
ISW	internal soliton wave;
FS	frequency shifts;
MFP	matched field processing;
3DHE	3D Helmholtz Equation models;
3DPE	3D Parabolic Equation models;
3DR	3D Ray-based models;
VMMPE	Vertical Modes and 2D Modal Parabolic Equation models;
VCMHR	Vertical Coupled Modes with Horizontal Rays models.

References

1. Weston D, Stevens K. Interference of wide-band sound in shallow water. *J. Sound Vib. 21(1):57–64.* **1972**.
2. Chuprov S. Interference structure of a sound field in a layered ocean. *Ocean Acoust., Curr. State. 71–91.* **1982**.
3. D'Spain GL, Kuperman WA. Application of waveguide invariants to analysis of spectrograms from shallow water environments that vary in range and azimuth. *J. Acoust. Soc. Am., 106(5):2454–2468.* **1999**.
4. Cockrell KL, Schmidt H. A relationship between the waveguide invariant and wavenumber integration. *J. Acoust. Soc. Am., 128(1):EL63–EL68.* **2010**.
5. Cockrell KL, Schmidt H. A modal Wentzel–Kramers–Brillouin approach to calculating the waveguide invariant for non-ideal waveguides. *J. Acoust. Soc. Am., 130(1):72–83.* **2011**.
6. Harrison CH. The relation between the waveguide invariant, multipath impulse response, and ray cycles. *J. Acoust. Soc. Am., 129(5):2863–2877.* **2011**.
7. Sell AW, Culver RL. Waveguide invariant analysis for modeling time-frequency striations in a range-dependent environment. *J. Acoust. Soc. Am., 130(5):EL316–EL322.* **2011**.
8. Song HC, Cho C. The relation between the waveguide invariant and array invariant. *J. Acoust. Soc. Am., 138(2):899–903.* **2015**.
9. Zhao ZD, Wu JR, Shang EC. How the thermocline affects the value of the waveguide invariant in a shallow-water waveguide. *J. Acoust. Soc. Am., 138(1):223–231.* **2015**.
10. Weng J, Li F, Guo Y. The sound field frequency-range interference patterns in deep water: theory and experiment. *Acta Acustica, 41(3):330–342.* **2016**.
11. Turgut A, Fialkowski LT, Schindall JA. Measured depth-dependence of waveguide invariant in shallow water with a summer profile. *J. Acoust. Soc. Am. Express Lett., 139(6):EL184–EL189.* **2016**.
12. Song W, Wang N, Gao D, Wang H, Hu T, Guo S. The influence of mode coupling on waveguide invariant. *J. Acoust. Soc. Am., 142(4):1848–1857.* **2017**.
13. Emmetière R, Bonnel J, Géhant M, Cristol X, Chonavel T. Understanding deep-water striation patterns and predicting the waveguide invariant as a distribution depending on range and depth. *J. Acoust. Soc. Am., 143(6):3444–3454.* **2018**.
14. Ianniello J. Recent developments in sonar signal processing. *IEEE Signal Proc. Magazine, 15(4):27-40.* **1998**.
15. Thode AM. Source ranging with minimal environmental information using a virtual receiver and waveguide invariant theory. *J. Acoust. Soc. Am., 108(4):1582-1594.* **2000**.
16. Kuperman WA, D'Spain GL. Ocean acoustic interference phenomena and signal processing. *Ocean Acoust. Interfer. Phenom. Signal Proc. 621.* **2002**.
17. Rouseff D, Spindel RC. Modeling the waveguide invariant as a distribution. *AIP Conf. Proc., Amer. Inst. Phys. 621:137-150.* **2002**.
18. Baggeroer AB. Estimation of the distribution of the interference invariant with seismic streamers. *AIP Conf. Proc., Amer. Inst. Phys. 621:151-170.* **2002**.
19. Yang T. Beam intensity striations and applications. *J. Acoust. Soc. Am., 113(3):1342-1352.* **2003**.
20. Heaney KD. Rapid geoacoustic characterization using a surface ship of opportunity. *IEEE J. Oceanic Engrg., 29(1):88-99.* **2004**.
21. Cockrell KL, Schmidt H. Robust passive range estimation using the waveguide invariant. *J. Acoust. Soc. Am., 127(5):2780-2789.* **2010**.

22. Rouseff D, Zurk LM. Striation-based beam forming for estimating the waveguide invariant with passive sonar. *J. Acoust. Soc. Am. Express Lett., 130:76–81.* **2011**.
23. Harrison CH. The relation between the waveguide invariant, multipath impulse response, and ray cycles. *J. Acoust. Soc. Am., 129(5):2863-2877.* **2011**.
24. Emmetiere R, Bonnel J, Gehant M, Cristol X, Chonavel Th. Understanding deep-water striation patterns and predicting the waveguide invariant as a distribution depending on range and depth. *J. Acoust. Soc. Am., 143(6):3444-3454.* **2018**.
25. Emmetiere R, Bonnel J, Cristol X, Gehant M, Chonavel T. Passive source depth discrimination in deep-water. *IEEE J. Select. Topics Signal Process., 13(1):185-197.* **2019**.
26. Kuznetsov GN, Kuzkin VM, Pereselkov SA. Spectrogram and localization of a sound source in a shallow sea. *Acoust. Phys., 63(4):449-461.* **2017**.
27. Ehrhardt M, Pereselkov SA, Kuz'kin VM, Kaznacheev I, Rybyanets P. Experimental observation and theoretical analysis of the low-frequency source interferogram and hologram in shallow water. *J. Sound Vibr. 544:117388.* **2023**.
28. Pereselkov S, Kuz'kin V, Ehrhardt M, Tkachenko S, Pereselkov A, Ladykin N. Application of Fractional Fourier Transform to Hologram Formation of a Moving Acoustic Source. *Fractal Fract. 9, 715.* **2025**
29. Pereselkov S, Kuz'kin V, Ehrhardt M, Tkachenko S, Rybyanets P, Ladykin N. Use of Interference Patterns to Control Sound Field Focusing in Shallow Water. *J. Mar. Sci. Eng. 11, 559.* **2023**
30. Baggeroer AB, Kuperman WA, Mikhalevsky PN. An overview of matched field methods in ocean acoustics. *IEEE J. Oceanic Eng., 18(4):401-424.* **1993**.
31. Tolstoy A. Matched Field Processing for Underwater Acoustics *World Scientific. Singapore. 18(4):1-212.* **1993**.
32. Jackson DR, Ewart TE. The effect of internal waves on matched-field processing. *J. Acoust. Soc. Amer., 96(5):2945-2955.* **1994**.
33. Baggeroer AB, Kuperman WA, Schmidt H. Matched field processing: Source localization in correlated noise as an optimum parameter estimation problem. *J. Acoust. Soc. Amer., 83(2):571-587.* **1998**.
34. Baggeroer AB. Why did applications of MFP fail, or did we not understand how to apply MFP?. *Proc. 1st Int. Conf. and Exhibition. Underwater Acoustics / Eds. Papadakis J.S., Bjorno L. Corfu Island, Greece :41–49.* **2013**.
35. Kuz'kin VM, Pereselkov SA, Zvyagin VG, Malykhin AYu, Prosovetskiy DYu. Intense internal waves and their manifestation in interference patters of received signals on oceanic shelf. *Phys. Wave Phenom., 26(2):160-167.* **2018**.
36. Badiey M, Kuz'kin VM, Lyakhov GA, Pereselkov SA, Prosovetskiy DYu, Tkachenko SA. Intense internal waves and their manifestation in the interference patterns of received signals on oceanic shelf. Part II *Phys. Wave Phenom., 27(4):313-319.* **2019**.
37. Kaznacheeva ES, Kuz'kin VM, Pereselkov SA. Interferometric processing of hydroacoustic information in the presence of intense internal waves. *Phys. Wave Phenom., 29(3):278-284.* **2021**.
38. Badiey M, Kuz'kin VM, Pereselkov CA, Ladykin NV, Malykhin AYu, Tkachenko SA. Robustness of holographic processing of hydroacoustic signals in the presence of intense internal waves. *Phys. Wave Phenom., 31(5):346-354.* **2023**.
39. Badiey M and SWARM'95 group. Cruise Report. Ocean Acoustic Experiments in Support of Shallow Water Acoustic Remote Measurements (SWARM). *University of Delaware P. 72.* **1995**.
40. Apel JR, Badiey M, Chiu C-S, Finette S, Headrick RH, Kemp J, Lynch JF, Newhall AE, Orr MH, Pasewark BH, Tielburger D, Turgut A, von der Heydt K, Wolf SN. An overview of the SWARM 1995 shallow-water internal wave acoustic scattering experiment. *IEEE J. Ocean. Engrg., 22:465-500.* **1997**.
41. Badiey M, Katsnelson BG, Lynch JF, Pereselkov SA, Siegmann W. Measurement and modeling of three-dimensional sound intensity variations due to shallow-water internal waves. *J. Acoust. Soc. Am., 117(2):613–625.* **2005**.
42. Serebryany AN. Manifestation of the properties of solitons in internal waves on the shelf. *Izv. Acad. Sci. USSR, Phys. Atmosphere Ocean, 29(2):285-293.* **1993**.
43. Ostrovsky LA, Stepanyants YuA. Do internal solitons exist in the ocean? *Reviews of Geophysics 27:293-310.* **1989**.
44. Konyaev KV, Sabinin KD. Waves inside the ocean. *St. Petersburg, Gidromet. Publ., 271 p.* **1992**.
45. Katsnelson BG, Pereselkov SA. Low-frequency horizontal acoustic refraction caused by internal wave solitons in a shallow sea. *Acoust. Phys., 46(6):684-691.* **2000**.

46. Pereselkov S, Kuz'kin V, Ehrhardt M, Tkachenko S, Rybyanets P, Ladykin, N. Three-Dimensional Modeling of Sound Field Holograms of a Moving Source in the Presence of Internal Waves Causing Horizontal Refraction. *J. Mar. Sci. Eng. 11, 1922.* **2023**
47. Pereselkov S, Kuz'kin V, Ehrhardt M, Tkachenko S, Pereselkov A, Ladykin N. Influence of Intense Internal Waves Traveling Along an Acoustic Path on Source Holographic Reconstruction in Shallow Water. *J. Mar. Sci. Eng. 13, 1409.* **2025**
48. Lin Y-T, Porter MB, Sturm F, Isakson MJ, Chiu C-S. Introduction to the special issue on three-dimensional underwater acoustics. *J. Acoust. Soc. Am., 146(3):1855–1857.* **2019**.
49. Liu W, Zhang L, Wang W, Wang Y, Ma S, Cheng X, Xiao W. A three-dimensional finite difference model for ocean acoustic propagation and benchmarking for topographic effects. *J. Acoust. Soc. Am., 150(2):1140–1156.* **2021**.
50. Tu H, Wang Y, Liu W, Yang C, Qin J, Ma S, Wang X. Application of a Spectral Method to Simulate Quasi-Three-Dimensional Underwater Acoustic Fields. *J. Sound Vibr., 545:117421.* **2023**.
51. Larsson E, Abrahamsson L. Helmholtz and parabolic equation solutions to a benchmark problem in ocean acoustics. *J. Acoust. Soc. Am., 113(5):2446–2454.* **2003**.
52. Smith KB, Tappert FD. UMPE: The University of Miami Parabolic Equation Model. *Version 1.1 "MPL Technical Memorandum 432", P. 96.* **1993**.
53. Tappert FD. The parabolic approximation method. Lecture Notes in Physics, V. 70, Eds. J.B. Keller, J.S. Papadakis, Eds., Wave Propagation and Underwater Acoustics, *Springer-Verlag, New York, Chapter 5, pp. 224-287.* **1977**.
54. Lin Y-T. Three-dimensional boundary fitted parabolic-equation model of underwater sound propagation. *J. Acoust. Soc. Am., 146(3):2058–2067.* **2019**.
55. Heaney KD, Campbell RL. Three-dimensional parabolic equation modeling of mesoscale eddy deflection. *J. Acoust. Soc. Am., 139(2):918–926.* **2016**.
56. Ivansson S. Local accuracy of cross-term corrections of three-dimensional parabolic-equation models. *J. Acoust. Soc. Am., 146(3):2030–2040.* **2019**.
57. Lee K, Seong W, Na Y. Three-dimensional Cartesian parabolic equation model with higher-order cross-terms using operator splitting, rational filtering, and split-step Padé algorithm. *J. Acoust. Soc. Am., 146(3):2030–2040.* **2019**.
58. Lee K, Seong W, Na Y. Split-step Padé solver for three dimensional Cartesian acoustic parabolic equation in stair-step representation of ocean environment. *J. Acoust. Soc. Am., 146(3):2050–2057.* **2019**.
59. Porter MB. Beam tracing for two- and three-dimensional problems in ocean acoustics. *J. Acoust. Soc. Amer., 146(3):2016–2029.* **2019**.
60. Porter MB. Bellhop3d User Guide. *La Jolla, CA: Heat, Light, and Sound Research, Inc.* **2016**.
61. Collins MD. The adiabatic mode parabolic equation. *J. Acoust. Soc. Am. 94:2269–2278.* **1993**.
62. Trofimov MY, Kozitskiy S, Zakharenko A. A mode parabolic equation method in the case of the resonant mode interaction. *Wave Motion, 58:42–52.* **2015**.
63. Petrov PS, Sturm F. An explicit analytical solution for sound propagation in a three-dimensional penetrable wedge with small apex angle. *J. Acoust. Soc. Amer., 139(3):1343–1352.* **2016**.
64. Kohler W, Papanicolaou GC. Wave propagation in a randomly inhomogeneous ocean. In: Keller JB Papadakis JS (Eds.), Wave Propagation and Underwater Acoustics *Lecture Notes in Physics, Springer, 70:153–223.* **1977**.
65. Dozier LB, Tappert FD. Mode coupling – surface roughness. *J. Acoust. Soc. Amer., 63(2):353–365.* **1978**.
66. Dozier LB, Tappert FD. Mode coupling – bottom roughness. *J. Acoust. Soc. Amer., 63(2):365–370.* **1978**.
67. Fawcett JA. Coupled-mode equation refinements. *J. Acoust. Soc. Amer., 91(4):2052–2061.* **1992**.
68. Trofimov AS, et al. Formal derivations of mode coupling equations. *J. Mar. Sci. Eng., 11(4):797–812.* **2023**.
69. Colosi JA, Flatté SM. Mode coupling by internal waves. *J. Acoust. Soc. Amer., 100(6):3607–3620.* **1996**.
70. Zhou JX, Zhang XZ, Rogers PH. Resonant interaction of sound wave with internal solitons in the coastal ocean. *J. Acoust. Soc. Amer., 90(4):2042–2054.* **1991**.
71. Preisig JC, Duda TF. Coupled acoustic mode propagation through continental-shelf internal solitary waves. *IEEE J. Oceanic Eng., 22(3):256–269.* **1997**.
72. Duda TF, Preisig JC. A modeling study of acoustic propagation through moving shallow-water nonlinear wave packets. *IEEE J. Oceanic Eng., 24(1):16–32.* **1999**.
73. Duda TF. Acoustic mode coupling by nonlinear internal wave packets in a shelf break front area. *IEEE J. Oceanic Eng., 29(1):118–125.* **2004**.

74. Higham CJ, Tindle CT. Coupled perturbed modes and internal solitary waves. *J. Acoust. Soc. Amer., 113(5):2515–2522.* **2003**.
75. Feng L, Goff JA, Yang B. Nonlinear internal-wave interaction. *J. Acoust. Soc. Amer., 116(4):2300–2310.* **2004**.
76. Colosi JA. Acoustic mode coupling induced by shallow water nonlinear internal waves: sensitivity to environmental conditions and space–time scales of internal waves. *J. Acoust. Soc. Amer., 124(3):1452–1464.* **2008**.
77. Yang TC. Acoustic mode coupling induced by nonlinear internal waves: evaluation of the mode coupling matrices and applications. *J. Acoust. Soc. Amer., 135(2):610–625.* **2014**.
78. Jensen FB, Kuperman WA, Porter MB, Schmidt H, Tolstoy A. Computational Ocean Acoustics. *Springer.* **2011**.
79. Brekhovskikh LM, Lysanov YP. Fundamentals of Ocean Acoustics. *Springer.* **2013**.